# Recent Seismic Activity in the Bejaia–Babors Region (Northeastern Algeria): The Case of the 2012–2013 Bejaia Earthquake Sequences

OUALID BOULAHIA,[1] ISSAM ABACHA,[1] ABDELKARIM YELLES-CHAOUCHE,[1] HICHEM BENDJAMA,[1] ABDELAZIZ KHERROUBI,[1] YAHIA MOHAMMEDI,[1] CHAFIK AIDI,[1] and ADEL CHAMI[1]

*Abstract*—From November 2012 to May 2013, the coastal region of Bejaia (northeastern Algeria), experienced three distinct seismic sequences in about 6 months. The first one was on 28 November 2012 started with a mainshock of magnitude $M_w = 5.1$, and the second one occurred on 22 February 2013, a few kilometers southeast from the first one and culminated with a magnitude $M_w = 4.3$ earthquake. The last sequence comprised two shocks of moderate magnitude: a $M_w$ 5.2 event on 19 May 2013, followed by a $M_w$ 5.0 event on 26 May. Earthquakes were relocated using the double-difference method with differential times derived from phase-picked data and waveform cross-correlation delays. We compiled a dataset of 252 accurately relocated events that are associated with focal mechanism solutions consistent with a near-vertical, right-lateral strike-slip fault striking NW–SE. The data analysis is coherent with a new fault extending over 35 km from the Gulf of Bejaia to the northeast of Kherrata. This newly discovered active fault, we name it the Babors Transverse Fault, appears to be segmented in four segments (S1–S4) evidenced by separate earthquake clusters. Static Coulomb stress changes and the spatiotemporal evolution of seismicity suggest static stress triggering, with the rupture first activated in the S1 segment in the northwest, migrating to S2, and terminating in S3 and S4 in the southeast. Stress tensor inversion from focal mechanisms implies that the dominant local stress field is a pure strike-slip regime, with N–S maximum horizontal compression in good agreement with the velocity field displaying reorientation compared to the oblique convergence of Africa–Eurasia. In this study, the newly identified Babors Transverse and Tizi N'Berber–Darguinah faults, in association with the NNW–SSE offshore active fault of the Greater Kabylian block (in the north) and the NNW–SSE right-lateral strike-slip Lâalam fault (in the south), form an en echelon fault system that acts as a transfer zone between offshore thrust faulting and the Ghardimaou–North Constantine strike-slip fault.

## 1. Introduction

The Bejaia–Babors region is a coastal mountain region in northeastern Algeria, located 200 km east of Algiers. The mountains of the Babors belong to the external zones of the Tellian chain overhanging the bay of Bejaia. The Babors chain outlines the region between the two Paleozoic Kabylian blocks of the Internal Domain (Greater and Lesser Kabylian blocks) (Durand-Delga 1969) (Fig. 1a, b).

The convergence of the African and Eurasian plates in the Ibero-Maghrebian domain results in a continuous occurrence of earthquakes of low to moderate magnitude (Udias & Buforn 1994) with a few strong ($6 \leq M_w \leq 6.9$) to major earthquakes ($7 \leq M_w \leq 7.9$): e.g., in the Southern Alboran Sea in 2016 ($M_w$ 6.4) (Buforn et al. 2017), Hoceima (Morocco) in 1994 ($M_w$ 6.0) and 2004 ($M_w$ 6.4) (Akoglu et al. 2006; Cakir et al. 2006; Kariche et al. 2017; Tahayt et al. 2009), Asnam (Algeria) in 1980 ($M_w$ 7.3) and Boumerdes 2003 ($M_w$ 6.8) (Ayadi et al. 2008; Meghraoui et al. 2004; Ouyed et al. 1981; Philip & Meghraoui 1983; Yelles-Chaouche et al. 2004), and in the eastern part of the Ibero-Morocco region in 1960 ($M_b$ 6.1), 1964 ($M_w$ 6.5), and 1969 ($M_w$ 7.8) (Buforn et al. 2020).

In northeastern Algeria, many small to moderate earthquakes occurred in the last 10 years. We registered: the 2010 Beni-Ilmane earthquake sequence which ruptured two distinct and adjacent NNE–SSW

[1] CRAAG, Centre de Recherche en Astronomie Astrophysique et Géophysique, Route de L'Observatoire B.P. 63 Bouzaréah, 16340 Algiers, Algeria. E-mail: oualid.boulahia@craag.edu.dz; o.boulahia@craag.dz; i.abacha@craag.dz; a.yelles@craag.dz; h.bendjama@craag.dz; aziz.kherroubi@gmail.com; yahyouhe@yahoo.fr; c.aidi@craag.dz; a.chami@craag.dz
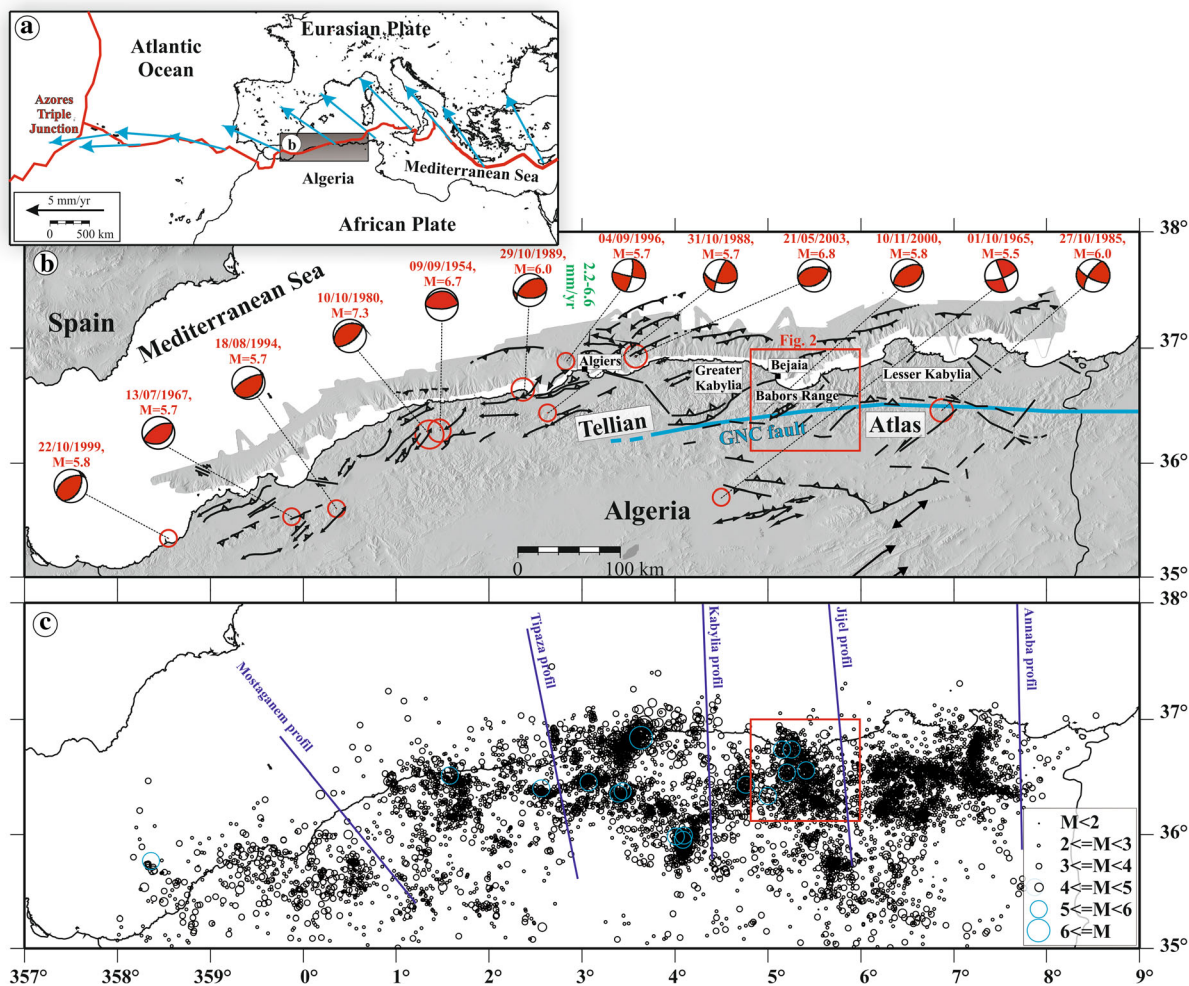
Figure 1

**a** Tectonic outline of the Mediterranean region. The grey surface frames the northern Algeria part. Predicted velocities along the Eurasia–Africa Plate boundary (blue arrows from Nocquet et al. 2006). **b** Seismotectonic map of northern Algeria, displaying the main active faults delineated in the Tellian Atlas (inspired by Domzig 2006; Kherroubi et al. 2009; Meghraoui 1988; Vila 1980; Yelles-Chaouche et al. 2009b) as well as the focal mechanisms of earthquakes of $M \geq 5.5$ (Harvard: https://www.globalcmt.org/CMTsearch.html). The blue solid line shows the major active Ghardimaou–North Constantine (GNC) fault compelled by geodetic data (Bougrine et al. 2019). **c** Northern Algeria seismicity between 1900 and 2020 (CRAAG catalog). Five purple lines indicate the location of the SPIRAL wide-angle profiles

left-lateral strike-slip fault segments and an E–W reverse fault segment (Abacha et al. 2014; Yelles-Chaouche et al. 2013a); the 2015 Ain Azel earthquake which broke two E–W V-shaped right-lateral strike-slip fault segments (Abacha & Yelles-Chaouche 2019; Chami et al. 2019), the 2017 earthquake sequence along the main Mcid-Aïcha Debbagh Fault (Bendjama et al. 2021), and the 2019 Jijel earthquake which ruptured an ∼ EW thrust fault

segment offshore of the Jijel region (Yelles-Chaouche et al. 2021).

From regional seismicity analysis in northern Algeria (Fig. 1b, c), we notice that the Bejaia–Babors region belongs to a transition zone (gray square in Fig. 2a), between a wide fold-and-thrust belt (∼ 100-km-wide region) in western and central parts of northern Algeria characterized by the highest-magnitude earthquakes, and a zone of relatively

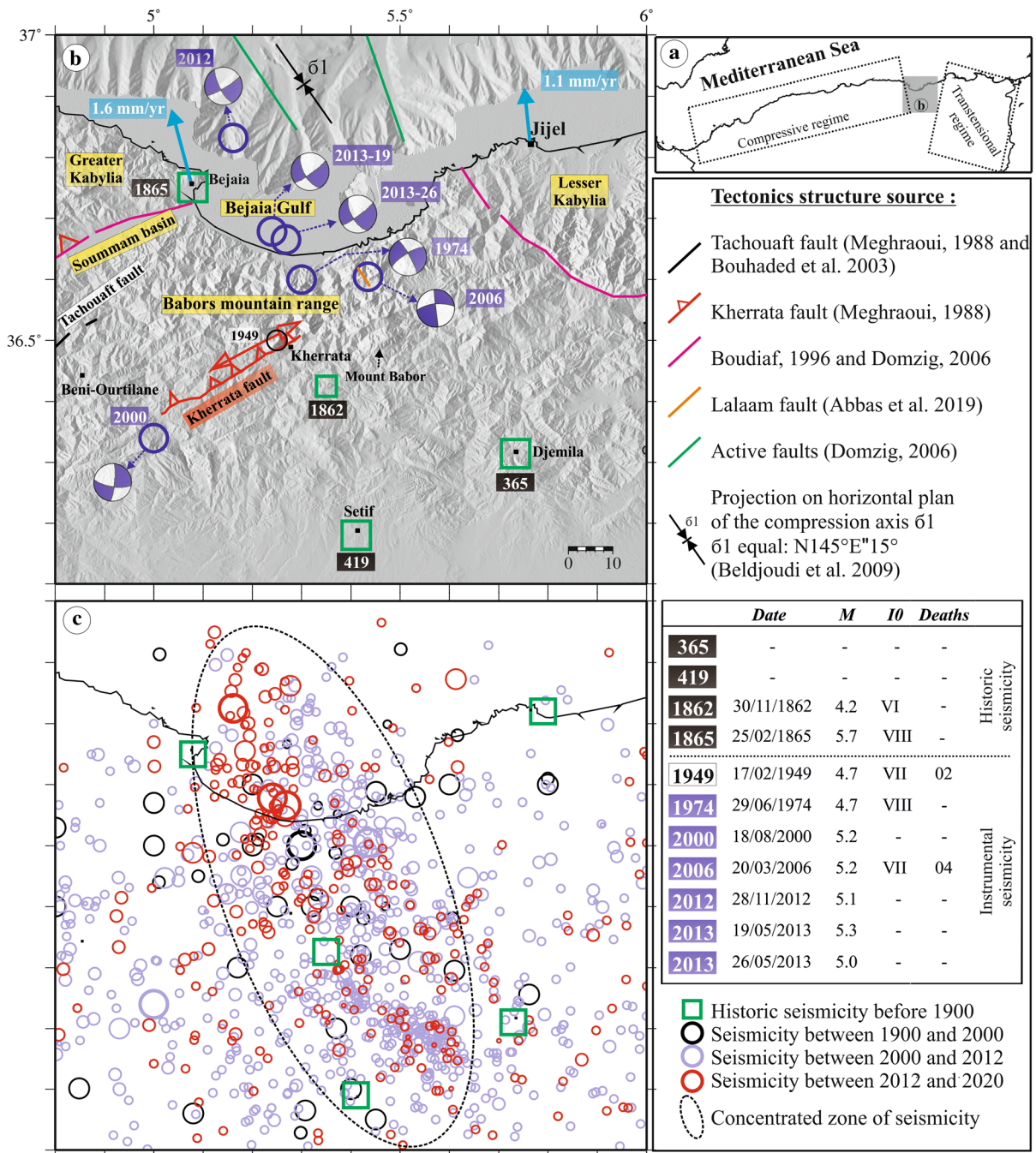Figure 2
**a** The dashed rectangles delineate domains characterized by relatively uniform tectonic regimes (from Serpelloni et al. 2007). **b** Seismo-tectonic map of the Babors zone and Setif region. The focal solution of the 1974 earthquake is obtained from Hatzfeld (1978). **c** Seismic events were detected in the region from 1900 to 2020, and the largest historical earthquakes (CRAAG catalog)

distributed deformation in the eastern part marked by low to moderate magnitude mainly related to strike-slip faulting (Abacha 2015; Abacha & Yelles-Chaouche 2019; Bougrine et al. 2019; Buforn et al. 2004; Harbi et al. 2003; Meghraoui & Pondrelli 2012; Serpelloni et al. 2007; Soumaya et al. 2018).

The Bejaia–Babors region is delimited between two major structures: the offshore thrust fault system in the north marking the Europe–Africa plate boundary (Bird 2003) and the Ghardimaou–North Constantine Fault (GNC) in the south (Fig. 1b). In the context of convergent margins, accommodation of the oblique plate motion develops new strike-slip faults or activates inland crustal weakness (Cooke et al. 2020). Slip partitioning arising from oblique subduction is typically attributed to margin-parallel strike-slip crustal faults (Stanton-Yonge et al. 2016 and reference therein). However, the Algerian margin transverse faults referred to as faults striking 30° to 60° away from the trend of the margin (Stanton-Yonge et al. 2016) remain poorly known due to the lack of additional marine surveys to the previous MARADJA program (Yelles-Chaouche and Maradja Team 2006). Therefore, from a seismology point of view, the study of 2012–2013 sequences allowed us to investigate such structure striking $\sim 50°$ from the margin and to understand its kinematics.

The Bejaia–Babors region is a seismic zone where little information was known until recently due to insufficient coverage of seismic stations and because of a lack of seismic and geological investigations. The main information related to this area comes from historical catalogs. For a long time, several authors have suggested that the Kherrata reverse fault is primarily responsible for the seismic activity of the region (Beldjoudi et al. 2009; Bouhadad et al. 2003; Meghraoui 1988; Harbi et al. 1999; Rothé 1950; Yelles-Chaouche et al. 2006), while all recent focal mechanisms show strike-slip faulting.

The recent installation of the Algerian Digital Seismic Network (ADSN; Yelles-Chaouche et al. 2013b) makes it possible to progressively discover the focus of many epicentral areas, such as the bay of Bejaia and the Lâalam area in the Babors region where a moderate event occurred in 2006 (Abbes et al. 2019; Beldjoudi et al. 2009). This earthquake damage the center of Lâalam city with four deaths, 68

injured, and more than 40 housing units destroyed. Field investigations revealed that these casualties were caused by an earthquake-induced landslide (Guemache et al. 2010). The decade 2010–2020 had been a more fruitful period to investigate the seismic activity of the Bejaia–Babors region due to the occurrence of several moderate events (mainly the sequences of 2012–2013). Yet, valuable small events had given a coherent understanding of the complex seismotectonic zone.

The primary objective of this study, which focuses mainly on the seismic sequences of 2012–2013, is first to analyze the spatiotemporal distribution of hypocenters located with high precision, then to identify the connection between the fault system and its kinematics. The analysis provides insights into the rupture process along the newly identified major transverse fault (the Babors Transverse Fault) on a well-resolved scale for the first time through the conjugate action of static stress and fluid-driven process. The results are integrated into a new regional kinematical frame, taking into account the previous studies. The stress change and fault segment interactions are presented to be incorporated in realistic seismic hazard assessment and risk mitigation, near one of the major cities of Northern Algeria.

## 2. Seismotectonic Setting

The Bejaia–Babors region situated close to the African and Eurasian plate boundary is among the active seismic zones in the Western Mediterranean (Udias & Buforn 1994). Along this border, the deformation is attributed to the anticlockwise rotation of Africa–Eurasia (Serpelloni et al. 2007). The line from the Azores triple junction in the west (Atlantic Ocean) to the Maghrebides belt in the east (Fig. 1a) crosses different tectonic regimes: respectively extensive, strike-slip, and finally compressive tectonic regimes.

The Algerian margin formed through the back-arc opening of the Algerian Basin in the Mediterranean Sea results from the rollback of the Tethys slab (Spakman & Wortel 2004). Compressional seismic activity recorded both inland and at sea indicates that this margin might be transitioning from a passive to

an active stage through an inversion process (Domzig 2006; Yelles-Chaouche et al. 2009b; Hamai et al. 2015, 2018; Strzerzynski et al. 2010). Recently, Soumaya et al. (2018) showed that the present-day active contraction of the northern Algerian boundary is accommodated by E–W strike-slip faulting with a reverse component along the Eastern Tellian Atlas Mountains and by predominantly NE–SW-trending thrust faults with a strike-slip component in the Western Tellian Atlas.

In Algeria, the seismicity is concentrated in the Tellian region, a part of the Maghrebides belt (Fig. 1c). The zone is dominated by a transpressive regime (Meghraoui & Pondrelli 2012), with a compression direction oscillating between N–S and NW–SE (Soumaya et al. 2018). The structures accommodating this deformation are mainly oriented NE–SW (Fig. 1b) perpendicular to the direction of shortening (the El Asnam fault, Meghraoui 1988; the Boumerdes fault, Yelles-Chaouche et al. 2004). Serpelloni et al. (2007) showed that the Tellian Atlas accommodates 2.7 to 3.9 mm/year from the current Africa-Eurasia convergence. The hypothesis of a deformation band along the margin, which accommodates a substantial percentage of the Africa–Eurasia convergence [4.4 mm/year in western Algeria to 1.5 mm/year in eastern Algeria (Bougrine et al. 2019)], agrees with the seismicity distribution (Fig. 1c) and also with the marine geophysical surveys: MARADJA 1, MARADJA2/SAMRA (MARge Active "el DJAzaïr") (Yelles-Chaouche and Maradja Team 2006) launched in 2003 and SPIRAL (Sismique Profonde de la Region Algerienne) in 2009 (Yelles-Chaouche and the Spiral Team 2010, Fig. 1c).

In the study area, the 2012–2013 earthquakes occurred in the Gulf of Bejaia and the Babors mountain range, between the Greater Kabylia and Lesser Kabylia crustal blocks (Durand-Delga 1969). The former is part of the dislocated Alboran, Kabylia, Peloritan, and Calabria (AlKaPeCa) zones of the European margin (Bouillin 1986). The rate of local shortening is $\sim$ 1.6 mm/year, as measured in Bejaia city (Fig. 2b; Bougrine et al. 2019). The Babors mountain range trends generally E–W and extends for more than 100 km between Lesser Kabylia and the Soummam basin (Fig. 2b). It is characterized by folded Jurassic limestone belts that trend E–W to

WNW–ESW and by high mountains with peaks up to 2004 m (at Mount Babor) (Fig. 2b). The depressions between the limestone massifs are filled by Lower Cretaceous marls. However, the present-day topography and dominant structures are the results of a late orogenic stage (Dalloni report in Rothé 1950). Among the structural sets inherited in these basement rocks is a NW–SE major orthogonal tectonic accident at K'Frida (Gabert 1984); according to Leikine (1971), the direction of the sliding movement of K'Frida is right lateral. Likewise, Guiraud (1977) made the same observations in the neighboring High Plains.

The Babors mountain range shows relatively high seismic activity in comparison to other parts of Algeria (Abacha 2015; Abacha & Yelles-Chaouche 2019). The seismicity of the region is characterized by events mostly of small magnitude and of moderate magnitude. (Fig. 2c). Several active faults have been recognized in the region (Bouhadad et al. 2003; Harbi et al. 1999; Meghraoui 1988; Vila 1980). In the central part of the Babors mountain range, the active Kherrata Fault was the source of the Ms 4.7 Kherrata earthquake on 17 February 1949 (Meghraoui 1988; Rothé 1950). The Kherrata fault-related fold trends 70°, plunges to the north, and is either > 10 km long (Rothé 1950) or 40 km long (Meghraoui 1988). The 1949 earthquake produced a reverse movement that resulted in a 50-m-long surface rupture and a vertical displacement of 30 cm (Rothé 1950). Earthquakes in the Bejaia–Babors region are generally of moderate magnitude, although destructive events have occurred in the past. For example, a strong earthquake in AD 419 (Fig. 2b) is reported to have destroyed the Byzantine city of Sitifis (Guidoboni 1994; Harbi et al. 2003; Yelles-Chaouche et al. 2009a).

In the last decade, the Beni-Ourtilane earthquake of 10 November 2000 ($M_s = 5.7$) was the first well-studied event. It allowed identifying the NE–SW reverse Tachouaft fault located at the western end of the Babors mountain range (Abacha & Yelles-Chaouche 2019; Bouhadad et al. 2003; Meghraoui 1988). The second event studied in the Babors region was the Lâlaam earthquake on 20 March 2006 ($M_w$ 5.2). It was firstly attributed to a N–S sinistral strike-slip segment (Beldjoudi et al. 2009). The recently revised study attributes this event to a NNW–SSE-
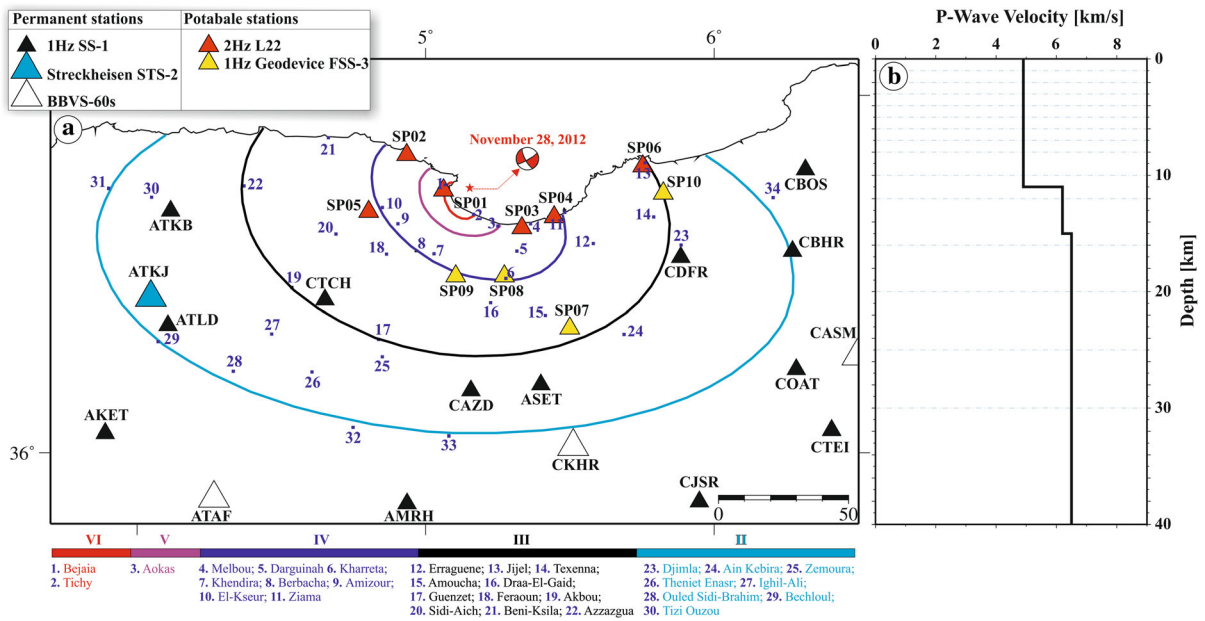
Figure 3

**a** Macro-seismic map of the 2012 first mainshock (modified from a CRAAG internal report) with the locations of stations in the seismic network and **b** the 1D velocity model (Beldjoudi et al. 2009) used in this study

striking fault (Lâlaam fault in Fig. 2b) (Abbes et al. 2019). Offshore investigations (e.g., Domzig 2006; Kherroubi et al. 2009; Yelles-Chaouche et al. 2009b) made during the Maradja 2 survey reveal offshore NW–SE to NNW–SSE-striking lineaments at the eastern side of the Greater Kabylian block that might correspond to active faults (Domzig 2006).

According to a survey of seismic activity in northern Algeria, the ADSN reveals a great number of small events in the Babors region. A quick look at the cloud of these events displays a major NW–SE trend (Fig. 2c) that cuts the Babors mountain range (Abacha 2015).

### 3. Data Acquisition and Velocity Model

The Bejaia earthquake sequences were recorded by permanent stations of the ADSN and a temporary (portable) network of 10 three-component seismic stations, deployed inland around the Gulf of Bejaia a few days after the first mainshock of 28 November 2012 (Fig. 3a). The temporary seismic network was

designed with a spacing of 10 to 40 km between stations. It contains two station types: six GEOS-TARS digitizers coupled to L22 ($f_0 = 2$ Hz) sensors and four GeoDevice EDAS-24IP digitizers coupled to GeoDevice FSS-3 ($f_0 = 1$ Hz) sensors. The permanent network consists of GeoDevice EDAS-24IP and Q330 digitizers coupled to GeoDevice BBVS-60s and Streckeisen STS-2 broadband sensors, as well as Q330 digitizers coupled to SS-1 ($f_0 = 1$ Hz) short-period sensors.

To minimize the uncertainties in event location, we tested four regional velocity models that have been used in previous studies of nearby earthquakes: the 2003 Boumerdes earthquake (Bounif et al. 2004), the 2006 Lâalam earthquake (Beldjoudi et al. 2009), the 2007 Mila earthquake (Semmane et al. 2012), and the 2010 Beni-Ilmane earthquake sequence (Yelles-Chaouche et al. 2013a). We also constructed a velocity model from two seismic profiles acquired during the SPIRAL (Sismique Profonde et Investigations Régionale du Nord de l'Algérie) project (Yelles-Chaouche 2010), namely the Kabylie profile (Aidi et al. 2018) located 100 km west of the Bejaia

epicentral area, and the Jijel profile (Mihoubi et al. 2014) located 50 km east of Bejaia (Fig. 1c). Both seismic profiles were used as a priori models for the 1D inversion algorithm VELEST (Kissling et al. 1994). The velocity model was built using the SPIRAL data, and it provided larger errors than the other models, probably due to the fact that the two transects were nonsuitable with the studied area. As regards the five models, the Lâalam model (Beldjoudi et al. 2009) provides the smallest residuals. This model consists of three layers, with P-wave velocities between 4.9–6.5 km/s and depths of 0–15 km (Fig. 3b) and a $V_p/V_s$ ratio equal to 1.75.

Between 28 November 2012 and 31 May 2013, a total of 345 events were identified, which were recorded by a minimum of four seismic stations. These events were located using the HYPOINVERSE software (Klein, 2002).

Following this first step, events with a root mean square (RMS) travel time residual of less than 0.30 s, location uncertainties in the horizontal (ERH) and vertical (ERZ) directions less than 2 km, and an azimuthal gap less than 180° are considered best-located events and are included in the final dataset. Of the 345 preliminary events, 328 (95%) meet these criteria. Three events of $M_d$ (duration magnitude) $\geq 3$ do not meet these conditions but have an RMS $\leq 0.35$ s. As these events were registered before the installation of the temporary network and are considered important, we retain them as the final dataset.

## 4. Methodology Analysis

This paper presents mainly the seismological study of the seismic sequences that took place in Bejaia–Babors (Northeastern Algeria). It focuses on the case of a series of four earthquakes and their aftershocks occurring between 2012 and 2013, supported by some small events occurring in the Babors region between 2014 and 2020. We applied a standard seismological procedure which includes hypocentral localization associated with a spatiotemporal evolution of seismicity; fault plane solution; stress field; changes in static Coulomb stress, etc. The different methodologies for data analysis are presented below.

### 4.1. Location, Relocation, and Focal Mechanism Techniques

Firstly, an absolute location of 345 events was performed using HYPOINVERSE software (Klein, 2002). Then, we perform a high-precision relocation of the seismic dataset by implementing a two-step process: (1) identification of multiplets using cross-correlation and (2) relocation of the identified families using the double-difference algorithm HypoDD (Waldhauser & Ellsworth 2000). These techniques have been widely employed to relocate earthquakes at local and regional scales (e.g., Hauksson & Shearer 2005; Waldhauser & Schaff 2008). In the first step, for all possible event pairs, we perform cross-correlations of the P-wave phase in the spectral domain from the vertical component of common seismological stations. The waveform windows are 256 samples long; they begin 100 samples before the P-wave pick, and are bandpass-filtered over 3–20 Hz. This procedure is used only for multiplet classification and not for the relocation process. Using relatively strict criteria, multiplet families are extracted by considering only the waveform pairs for which coherence is $\geq 0.7$ for at least four stations (four P phases). In the second step, we relocate the dataset with higher accuracy; we computed time delays between all possible earthquake pairs in each event family. We retain all estimated delays for P-wave pairs if the maximum value of the correlation function is $\geq 0.7$, then we exploit the ability of HypoDD to associate differential times derived from picked phases (P & S) and waveform cross-correlation delays.

Finally, focal mechanisms were calculated for events with at least 10 clear *P*-wave polarities using the SPHERA program (Rivera & Cisternas 1990). The code SPHERA provides two parameters, score and quality, which measure the misfit defined as the difference between polarities observed and predicted by the model. We employed as well the waveform modeling technique developed by Yagi and Nichimura (2011) to independently estimate the focal mechanism and other source parameters for the four

mainshocks. Nine broadband stations (27 components) were used to estimate the moment tensor solution. The observed raw data were corrected for seismometer responses and converted to ground velocity motion. We used 100–180 s of waveform data for each studied mainshock. The data were filtered in the relatively low frequencies (0.02–0.07 Hz) to mitigate the effect of the heterogeneity of the local velocity structure and to produce the best fit between observed and synthetic waveforms. Then, data were down-sampled with a 1-Hz rate. The Green's functions have been calculated using the discrete wavenumber method developed by Kohketsu (1985) for the velocity model based on the Lalaâm model (Beldjoudi et al. 2009) and used in the inversion of the observed three-component broadband waveforms (100–180 s). The moment tensor solutions have a quality factor assigned by the number of stations used during the inversion, and the goodness of fit between synthetic and observed data.

### 4.2. Spatiotemporal Evolution, Stress Tensor, and Coulomb Stress Change Triggering

To assess the behavior of the seismicity, we analyze the number of events as a function of time and the properties of earthquake clusters (Scholz 2002; Utsu 2002), such as foreshock–mainshock–aftershock sequences and earthquake swarm type. Aftershock activity decays with time according to a power law, empirically described by the modified Omori formula (Eq. 1):

$$N(t) = K/(t + c)^p, \qquad (1)$$

where $N(t)$ is the number of aftershocks per unit time, $t$ is the time since the mainshock, and $k$, $c$, and $p$ are constants (e.g., Utsu et al. 1995).

The estimated $p$ and $c$ values are considered to be the most important parameters in characterizing a mainshock–aftershock sequence (Utsu 1961, 1969). The value of $p$ is thought to be related to regional geology and tectonics (e.g., Kisslinger & Jones 1991; Utsu and Ogata 1995; Wiemer & Katsumata 1999).

To evaluate the consistency of the stress tensor with the kinematics of the seismogenic source and use the parameters of the stress tensor to estimate

Coulomb stress changes, we perform formal stress inversions for focal mechanisms of the 2012–2013 Bejaia sequence key events ($M_d \geq 3.0$) and a cluster of 11 events ($M_d \geq 3.0$) recorded between 2017 and 2020 (80 fault planes), following the technique of the TENSOR program (Delvaux & Sperner 2003) and using the Win-Tensor program (Delvaux 2012). The final stress tensor characterizes the tectonic stress regime in terms of the index $R'$: $R' = 0$–1 for extensional stress, 1–2 for strike-slip, and 2–3 for compression (Delvaux et al. 1997).

An important feature of seismogenesis is that earthquakes do not occur independently but interact with each other through their stress field (Scholz 2002). In cases of earthquake sequence, where several segments are involved in the rupture process, the spatial migration of seismicity is most probably enhanced by stress transfer. To identify this pattern, we explore the interaction between the activated segments. We assess the static stress changes caused by the 2012–2013 Bejaia earthquake sequences using the program Coulomb 3.4 (Stein et al. 1992; Toda et al. 1998). Using this method, we compute the stress change on a specified strike-slip fault, caused by a slip on a nearby source fault, within a homogenous elastic half-space. We assume a shear modulus of 32 GPa, Young's modulus of 80 GPa, and a Poisson's ratio of 0.25 which are typical values in the studied seismogenic layer (4–12 km) (Kariche et al. 2017; Khelif et al. 2018; Lin et al. 2011).

## 5. Results

### 5.1. Mainshock and Waveform Modeling

On 28 November 2012 at 23:15 (UTC), the first sequence among the four was started by an $M_d$ 5.1 offshore earthquake located 7 km NE of Bejaia city. This event was felt in the city and caused minor damage, mainly superficial cracks in old buildings. The isoseismal map (Fig. 3a) shows a general NW–SE trend, with a maximum intensity of VI (European Macroseismic Scale 1998) at the epicenter (CRAAG internal report). Waveform inversion resolves a seismic moment $M_0 = 5.3 \times 10^{16}$ Nm and a moment magnitude $M_w = 5.1$ (Table 1).

Table 1

*Computed locations, released moments, magnitudes, and focal mechanism solutions for the four mainshocks and those provided by different seismological observatories*

| Date | Oragnization | Origin Time | Magnitude | Localization Lat (°)N | lon (°)E | Depth (Km) | Nodal plan A strike (°) | dip (°) | rake (°) | Nodal plan B strike (°) | dip (°) | rake (°) | $M_0$ (N.m) | Solution |
|------|-------------|-------------|-----------|------|------|------|--------|-----|------|--------|-----|------|------|----------|
| 28/11/2012 | CRAAG (this study) p-waves polarities | 23 : 15 : 26.21 | $M_d = 5.1$ | 36.82 | 5.16 | 11.37 | 152.0 | 73.0 | -170.0 | 60.0 | 81.0 | -18.0 | - |  |
|  | CRAAG (this study) MT inversion | 23 : 15 : 26.21 | $M_w = 5.1$ | 36.82 | 5.16 | 11.37 | 134.8 | 62.5 | 164.3 | 232.5 | 75.6 | -151.5 | $5.30 * 10^{16}$ |  |
|  | GFZ | 23 : 15 : 30.59 | $M_w = 5.0$ | 36.70 | 5.07 | 10.0 | 157.0 | 37.0 | 170.0 | 255.0 | 84.0 | 53.0 | $3.60 * 10^{16}$ |  |
|  | Harvard CMT | 23 : 15 : 29.30 | $M_w = 5.0$ | 36.71 | 5.10 | 12.0 | 152.0 | 73.0 | -170.0 | 60.0 | 81.0 | -18.0 | $3.49 * 10^{16}$ |  |
|  | CSEM | 23 : 15 : 29.00 | $M_b = 4.9$ | 36.84 | 5.19 | 10.0 | - | - | - | - | - | - | - | - |
|  | IGN | 23 : 15 : 28.00 | $M_b = 5.2$ | 36.80 | 5.24 | 10.0 | - | - | - | - | - | - | - | - |
| 22/02/2013 | CRAAG (this study) p-waves polarities | 12 : 30 : 47.44 | $M_d = 4.3$ | 36.72 | 5.21 | 9.82 | 143.7 | 83.2 | 177.7 | 234.0 | 87.7 | 06.8 | - |  |
|  | CRAAG (this study) MT inversion | 12 : 30 : 47.44 | $M_w = 4.3$ | 36.72 | 5.21 | 9.82 | 125.3 | 73.3 | -163.1 | 30.3 | 73.8 | -17.4 | $0.32 * 10^{16}$ |  |
|  | GFZ | 12 : 30 : 48.20 | $m_b = 4.3$ | 36.77 | 5.32 | 10.0 | - | - | - | - | - | - | - | - |
|  | Harvard CMT | - | - | - | - | - | - | - | - | - | - | - | - | - |
|  | CSEM | 12 : 30 : 48.00 | $M_b = 4.5$ | 36.79 | 5.36 | 10.0 | - | - | - | - | - | - | - | - |
|  | IGN | 12 : 30 : 49.00 | $M_b = 4.8$ | 36.75 | 5.30 | 14.0 | - | - | - | - | - | - | - | - |
| 19/05/2013 | CRAAG (this study) p-waves polarities | 09 : 07 : 26.31 | $M_d = 5.3$ | 36.69 | 5.26 | 10.20 | 149.0 | 63.0 | -170.0 | 54.0 | 82.0 | -27.0 | - |  |
|  | CRAAG (this study) MT inversion | 09 : 07 : 26.31 | $M_w = 5.2$ | 36.69 | 5.26 | 10.20 | 135.5 | 67.6 | -176.7 | 44.3 | 87.0 | -22.4 | $7.50 * 10^{16}$ |  |
|  | GFZ | 09 : 07 : 29.80 | $M_w = 5.1$ | 36.80 | 5.23 | 12.0 | 146.0 | 89.0 | 178.0 | 236.0 | 88.0 | 1.0 | $4.70 * 10^{16}$ |  |
|  | Harvard CMT | 09 : 07 : 29.20 | $M_w = 5.2$ | 36.59 | 5.19 | 15.1 | 149.0 | 63.0 | -170.0 | 54.0 | 82.0 | -27.0 | $7.42 * 10^{16}$ |  |
|  | CSEM | 09 : 07 : 27.00 | $M_b = 5.1$ | 36.76 | 5.18 | 2.0 | - | - | - | - | - | - | - | - |
|  | IGN | 09 : 07 : 26.00 | $M = 5.5$ | 36.67 | 5.31 | 12.0 | - | - | - | - | - | - | - | - |
| 26/05/2013 | CRAAG (this study) p-waves polarities | 16 : 00 : 55.12 | $M_d = 5.0$ | 36.68 | 5.25 | 9.51 | 137.2 | 73.4 | -168.3 | 43.8 | 78.8 | -16.9 | - |  |
|  | CRAAG (this study) MT inversion | 16 : 00 : 55.12 | $M_w = 5.0$ | 36.68 | 5.25 | 9.51 | 95.2 | 64.9 | 140.7 | 204.4 | 55 | 31.2 | $3.80 * 10^{16}$ |  |
|  | GFZ | 16 : 00 : 55.40 | $m_b = 5.0$ | 36.73 | 5.28 | 8.0 | - | - | - | - | - | - | - | - |
|  | Harvard CMT | 16 : 00 : 56.80 | $M_w = 4.9$ | 36.66 | 5.17 | 20.1 | 101.0 | 38.0 | 144.0 | 221.0 | 69.0 | 58.0 | $3.03 * 10^{16}$ |  |
|  | CSEM | 16 : 00 : 56.00 | $M_b = 5.0$ | 36.71 | 5.19 | 12.0 | - | - | - | - | - | - | - | - |
|  | IGN | 16 : 00 : 55.00 | $M = 5.0$ | 36.73 | 5.30 | - | - | - | - | - | - | - | - | - |

The second earthquake ($M_d = 4.3$) occurred on 22 February 2013 at 12:30 (UTC) in Bejaia Bay, 10 km SE of the first mainshock. Waveform modeling gives a seismic moment $M_0 = 0.32 \times 10^{16}$ Nm and a moment magnitude $M_w = 4.3$.

Three months later, in May 2013, two earthquake sequences with mainshocks of duration magnitude $M_d = 5.3$ and $M_d = 5.0$ occurred near the village of Aokas (Bejaia coastline). These earthquakes were located to the southeast of the initial two events, along the same trend. The first was recorded on 19 May at 09:07 (UTC) and the second on 26 May at 16:00. Waveform modeling indicates the first event had a seismic moment $M_0 = 7.50 \times 10^{16}$ Nm and moment magnitude $M_w = 5.2$, and the second had $M_0 = 3.80 \times 10^{16}$ Nm and $M_w = 5.0$ (Table 1).

All solutions correspond to strike-slip motion, in agreement with that determined by international seismological agencies (Table 1).

## 5.2. Aftershock Distribution and Spatiotemporal Evolution

In total, seismic activity associated with the 2012–2013 Bejaia sequences lasted for 184 days. Over this time, 328 events previously filtered (several with magnitude $M_d \geq 3$) map onto a 35-km-long elongated cluster, trending NW–SE (Fig. 4a), all concentrated at depths of 4–12 km (Fig. 4b).

Seismicity over this period can be separated into four clusters, which are distinct in time and space. The earliest cluster (C1) occurred from 23:15 (UTC) on 28 November 2012 to 19:17 on 01 February 2013. The second cluster (C2) began at 03:15 on 12 February and ended at 06:16 on 08 May. Clusters C3 and C4 span from 09:07 on 19 May to 21:16 on 21 May, and from 16:00 on 26 May to 17:40 on 31 May, respectively.

Cluster C1 includes 46 events (colored green in Fig. 4a). This cluster can be considered as an ordinary mainshock–aftershock sequence, which began with the $M_w$ 5.1 event of 28 November 2012 and lasted 60 days. Following the mainshock, the cumulative number of events increased slightly and then stabilized (Fig. 4c), while event magnitudes decreased with time as expected (Scholz 2002) (Fig. 4d). Any rapid increase in the number of events is unlikely to have been recorded, given the absence

of nearby stations (the closest stations were two permanent stations, CTCH and CBOS, located 75 km from the mainshock 1).

Cluster C2 comprises 51 events (colored yellow in Fig. 4a) that define a foreshock–mainshock–aftershock sequence. The $M_w$ 4.3 mainshock occurred on 22 February 2013 and was preceded by three foreshocks on 12, 16, and 20 February 2013, of magnitudes $M_d = 2.1$, 3.3, and 3.5, respectively. The aftershocks occur in a small area ($\sim 2$ km$^2$) and show no clear geographical trend. During this crisis, the cumulative number of events increased rapidly even though the magnitudes are smaller than the first cluster, reflecting the improved coverage of the deployed mobile stations (Fig. 4c). The event magnitudes generally decreased in the days following the mainshock (Scholz 2002) (Fig. 4d).

Clusters C3 and C4 represent two successive mainshock–aftershock sequences and between them account for 70% of the event dataset. Cluster C3 (colored red in Fig. 4a) includes 58 events, while cluster C4 (colored blue in Fig. 4a) comprises 173 events. The two sequences have mainshocks of magnitudes $M_w = 5.2$ and $M_w = 5.0$, respectively. Although clusters C3 and C4 are distinct in time, they have similar spatial distributions (Fig. 4a, b). However, the relatively short time between mainshocks means that some aftershocks of C3 are likely to have occurred during the time of the C4 cluster. In Fig. 4b, events in each cluster show a V-shaped configuration. The left sub-cluster is more concentrated and contains the two mainshocks, whereas the right sub-cluster is more sparse and consists mainly of events belonging to cluster C4. Sharp increases in the cumulative number of events are seen following the mainshocks associated with each of these clusters (Fig. 4c), particularly for C4. However, C3 and C4 show a barely discernable decrease in event magnitude over time compared with clusters C1 and C2, but a zoom on the last two peaks' activity identifies the supposed decline in the kind of aftershock–mainshock sequences (Scholz 2002).

Next, in our temporal analysis, the maximum likelihood method was applied to estimate the value of $p$ of the modified Omori law in Eq. (1). To fit the decay of seismic activity after the first peak (C1), an exponent $p = 0.85$ is necessary (Fig. 5a), for the second peak (C2), an exponent $p = 1.11$ is required
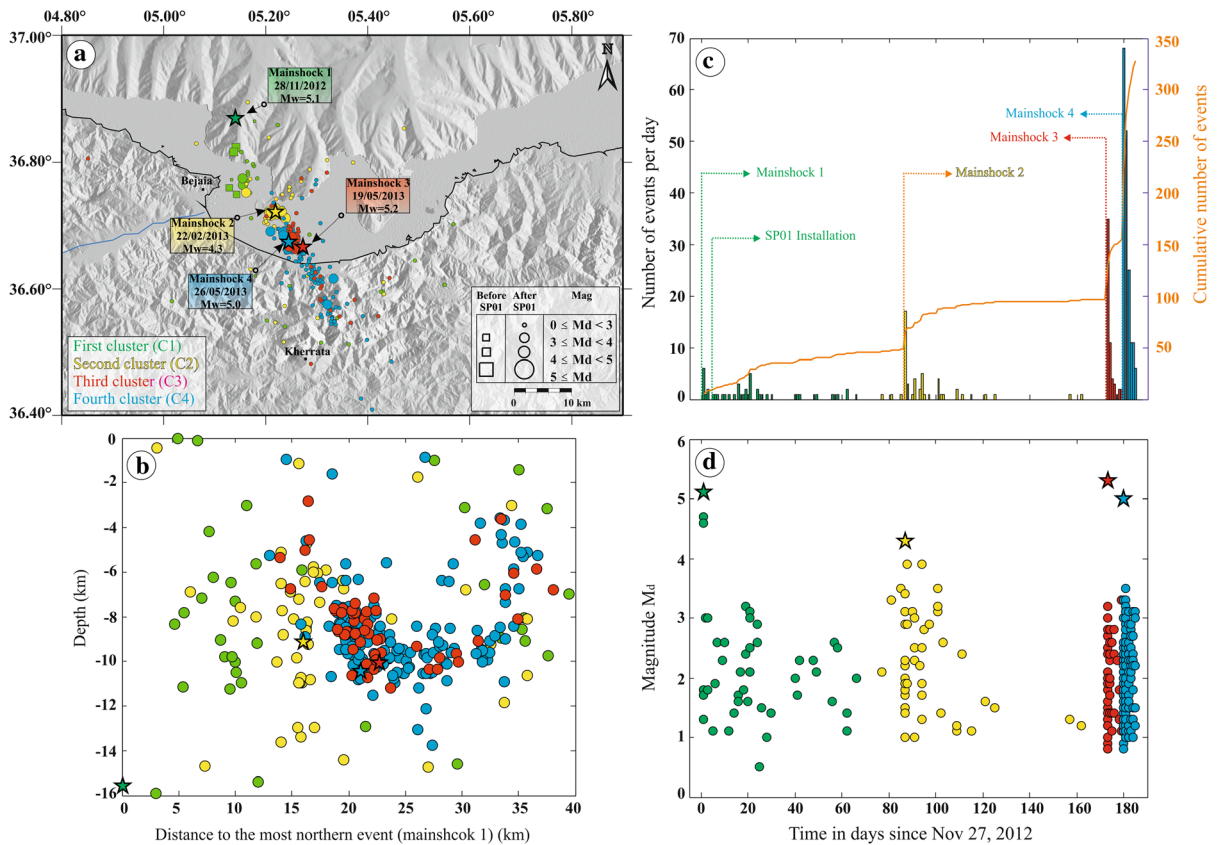
Figure 4

**a** Lateral distribution of the 328 best-located events. Green, yellow, red, and blue correspond to the first, second, third, and fourth seismic sequences, respectively. Squares represent epicenters located using data from the permanent network only (i.e., before installation of the temporary network). **b** Distance from the first mainshock (horizontal axis) vs. hypocenter depth (vertical axis) for our located data. The colors represent the sequence (time) in which the event occurred, consistent with **a**. **c** The cumulative number of events and number of events per day are associated with clusters C1–C4. **d** Temporal evolution of the event magnitudes

(Fig. 5b), and after the last two peaks of activity (C3 and C4), an exponent $p = 0.85$ is needed to describe the data (Fig. 5c). The exponents are within the normal range of different previous studies. Papazachos (1975) examined the temporal distribution of six aftershock sequences in Greece using the cumulative number method, revealing that the $p$ values are independent of the magnitude range and vary between 0.7 and 1.9. A median $p$ value of $\sim 1.1$ has been reported for the aftershock sequences in various regions worldwide, with a range of 0.6–2.5 (Utsu and Ogata, 1995), whereas Kisslinger and Jones (1991) reported $p$ values of 0.7–1.8 with a mean of 1.11 for shallow aftershock sequences in California. This parameter differs from sequence to

sequence based on the tectonic situation in the considered area, the higher $p$ value infers faster decay of aftershock activity. However, the $p$ value approaching a value of 1.0 indicates that the earthquake happened in a tectonically active region with an amount of stress dissipation. The value of the parameter $c$ can range from 0.01 days to over 1 day, and it is a dubious parameter (Utsu and Ogata, 1995) dependent on the rate of activity in the beginning part of the sequence. For the first peak (C1), it is difficult to estimate $c$ properly for the first mainshock–aftershock sequence, probably because of missing data shortly after the first mainshock when considerably small aftershocks are not seen on reported records. Given that 5 days of aftershock activity
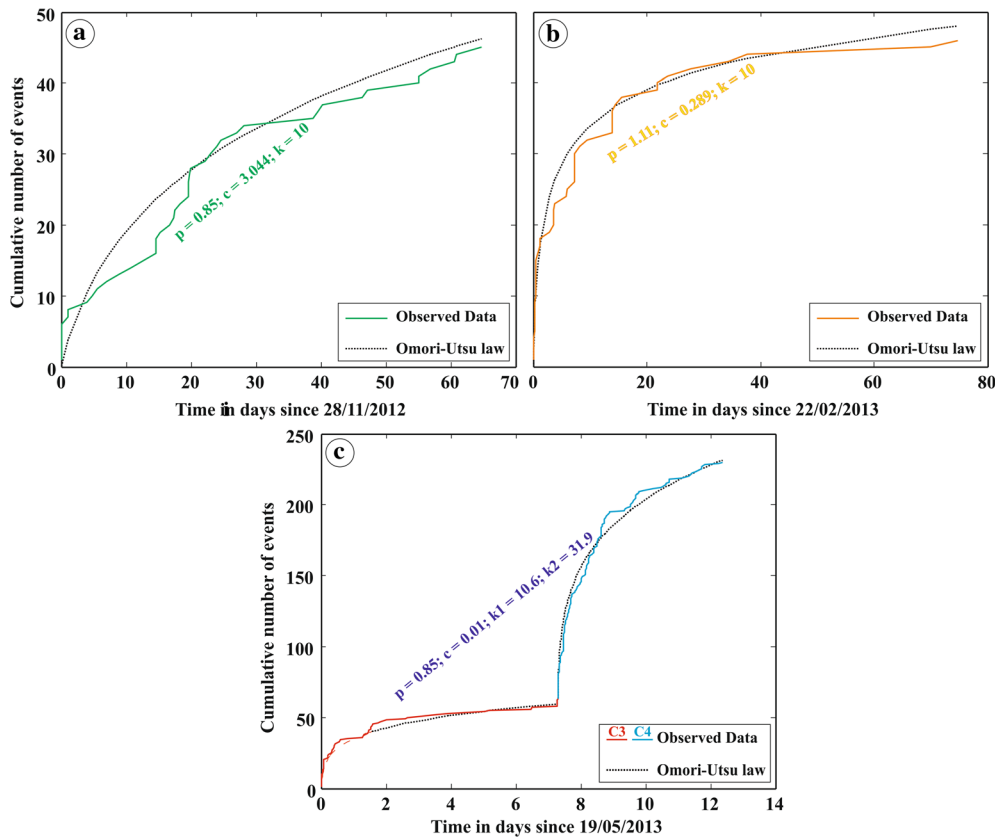
Figure 5

The Omori–Utsu law decay curve for the four seismic sequences and the cumulative number of events recorded with time during each sequence. **a** The first cluster (C1) of 70 days from the occurrence of the 28 November 2012 mainshock. **b** The second cluster (C2) of 80 days from the occurrence of the 22 February 2013 mainshock. **c** The third and fourth clusters (C3 and C4) of 14 days from the occurrence of the 19 May 2013 mainshock

lacked over this time, the calculated value of $c = 3.04$ (Fig. 5a) may be an overestimate.

The statistical analysis of the 2012–2013 sequences using 328 events ($0.5 \leq M_d \leq 5.3$) has provided interesting results concerning the spatial and temporal patterns that have emerged with the use of different methods. The presence of four separate seismicity phases in time and also in space have been analyzed along the NW–SE-striking fault with southeastward migration of the seismicity cluster.

### 5.3. Cluster Relocation and Focal Mechanisms

The HypoDD results demonstrate significant clustering of seismic events compared to those obtained by the HYPOINVERSE process. Out of

the initial 328 events, 252 are successfully relocated into five distinct clusters, with a spatial uncertainty in relative locations of less than 200 m for more than 82% of events (Fig. 6a). This spatial clustering of the relocated events (Fig. 6a) shows a linear feature that trends NW–SE and represents a rupture on five segments a total of $\sim 35$ km long, 3 km wide, and at a depth range between 6 and 12 km.

The green, yellow, and red clusters in Fig. 6a correspond to clusters C1, C2, and C3 (Fig. 4a), respectively, which are now more well-defined in space. The event relocations have also enabled us to better resolve cluster C4 as a V-shaped feature (cross-sectional view in Fig. 6a). The left side of the feature (colored blue in Fig. 6a) is a new family from the C3 cluster, and the right side is a new cluster shown in
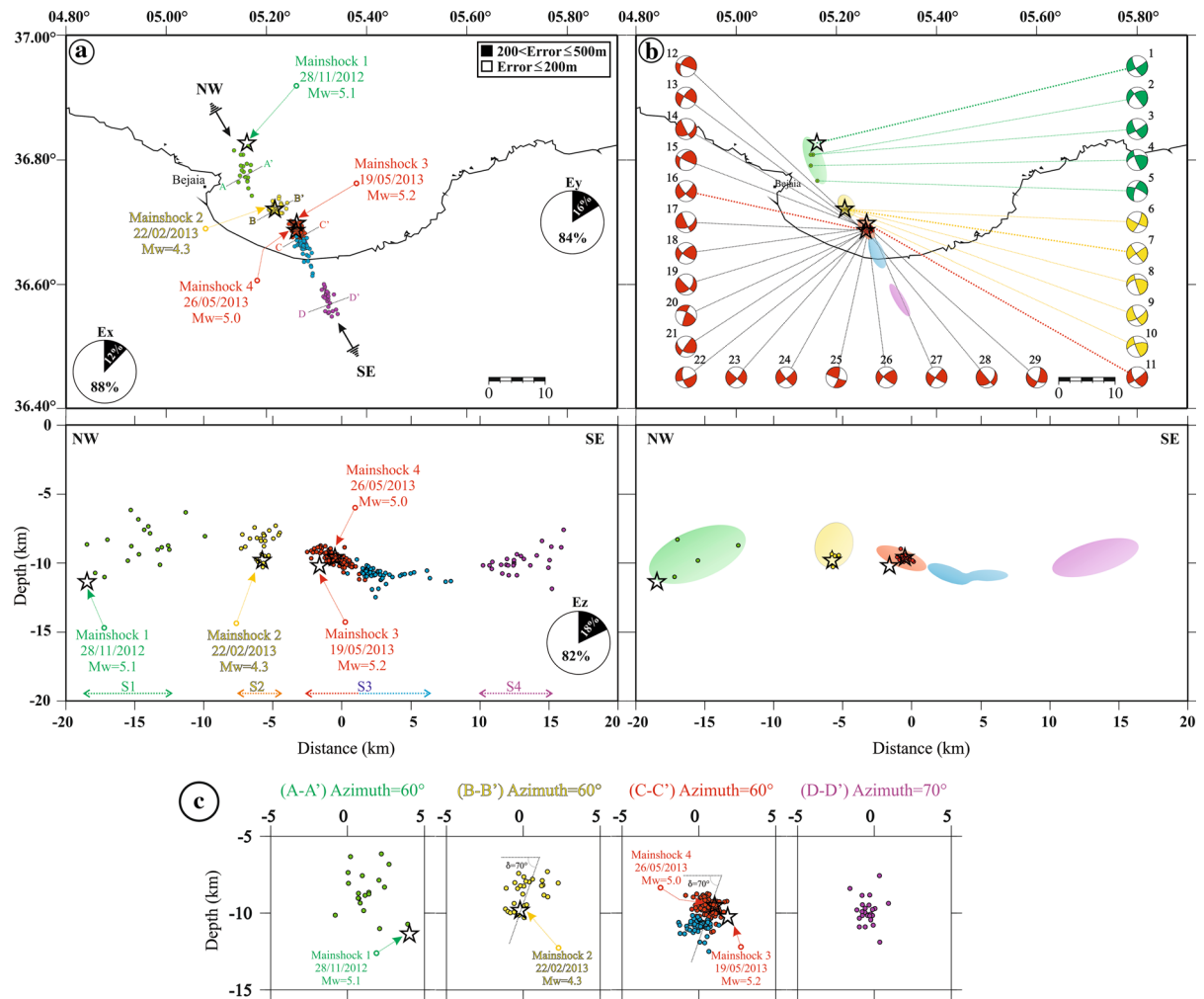
Figure 6

**a** Lateral and vertical distributions of the 252 relocated events. Colors relate to the multiplet clusters (families) as discussed in the text (Sect. 5.3). Green, yellow, red, blue, and purple relate to events of the first, second, third, fourth, and fifth multiplet clusters, respectively. Pie chart of relative relocating errors. **b** The lateral and vertical extent of the five multiplet clusters with locations and focal mechanisms for events with $M \geq 3$. Focal mechanisms are colored consistent with the multiplet cluster they represent (see **a**). The focal mechanisms are numbered as in Table 2. **c** Cross-sections perpendicular to each multiplet cluster

purple. In Fig. 6b, we depict the five multiplet clusters by ellipses that encompass most of the events in a given group. Each cluster was likely generated by activation of a separate fault segment (denoted S1–S4 in Fig. 6a) of the NW–SE-trending Babors Transverse Fault (BTF). The red and blue multiplet clusters (Fig. 6a, b) are an exception to this and are both associated with segment S3. The rupture was initiated in the shallow part of this segment (red cluster) and migrated deeper (blue cluster).

The results of focal mechanism solutions for events of magnitude $M_d \geq 3$ and having at least 10 P-wave polarities are displayed in Table 2 organized according to each cluster, and their polarities are shown in the Online Appendix. The focal mechanism solutions (Fig. 6b, Table 2, and Online Appendix) indicate strike-slip faulting, consistent with right-lateral slip on NW–SE-trending planes. The mean fault strike is $\sim 140°$, in agreement with the trend in

Table 2

*Fault plane solutions for the four mainshocks and 25 largest aftershocks ($M_d \geq 3$) of the 2012–2013 Bejaia seismic sequences and 2006–2020 ($M_d \geq 3$) earthquakes in the Babors region*

| | ID | No | Date (Ye/Mo/Dy) | Origin time (Hr:Mn:Se) | Md | Localization Lat (°)N | lon (°)E | Depth (Km) | Nodal plan A strike (°) | dip (°) | rake (°) | Nodal plan B strike (°) | dip (°) | rake (°) | Score (%) | Quality (%) |
|---|---|---|---|---|---|---|---|---|---|---|---|---|---|---|---|---|
| **The 2012-2013 Bejaia sequence main events** | | 01 | 12/11/28 | 23 : 15 : 26 | 5.1 | 36.82 | 5.16 | 11.37 | 152 | 73 | -170 | 60 | 81 | -18 | 100 | 69 |
| | | 02 | 12/11/28 | 23 : 20 : 17 | 4.7 | 36.80 | 5.15 | 8.30 | 143 | 90 | 143 | 233 | 53 | 0 | 100 | 76 |
| | C1 | 03 | 12/11/28 | 23 : 50 : 46 | 4.6 | 36.80 | 5.14 | 11.01 | 151 | 75 | -172 | 59 | 82 | -15 | 98 | 65 |
| | | 04 | 12/12/18 | 15 : 28 : 31 | 3.0 | 36.79 | 5.14 | 9.85 | 159 | 81 | 144 | 256 | 54 | 11 | 84 | 66 |
| | | 05 | 13/02/16 | 10 : 47 : 59 | 3.3 | 36.76 | 5.16 | 8.72 | 292 | 73 | -159 | 196 | 70 | -18 | 100 | 66 |
| | | 06 | 13/02/20 | 03 : 31 : 53 | 3.5 | 36.72 | 5.22 | 9.50 | 117 | 83 | -165 | 25 | 76 | 68 | 100 | 65 |
| | C2 | 07 | 13/02/22 | 12 : 30 : 47 | 4.3 | 36.72 | 5.21 | 9.82 | 144 | 83 | 178 | 234 | 88 | 7 | 96 | 71 |
| | | 08 | 13/02/22 | 18 : 36 : 05 | 3.4 | 36.72 | 5.21 | 10.31 | 163 | 85 | 138 | 258 | 48 | 7 | 100 | 86 |
| | | 09 | 13/02/23 | 15 : 30 : 53 | 3.9 | 36.71 | 5.22 | 9.45 | 153 | 77 | -160 | 58 | 70 | -14 | 89 | 61 |
| | | 10 | 13/03/01 | 18 : 43 : 17 | 3.9 | 36.71 | 5.21 | 9.37 | 160 | 81 | 156 | 254 | 66 | 10 | 87 | 67 |
| | | 11 | 13/05/19 | 09 : 07 : 26 | 5.3 | 36.69 | 5.26 | 10.20 | 149 | 63 | -170 | 54 | 82 | -27 | 90 | 72 |
| | | 12 | 13/05/19 | 09 : 15 : 44 | 3.0 | 36.68 | 5.25 | 9.63 | 11 | 89 | 136 | 202 | 46 | 1 | 100 | 66 |
| | | 13 | 13/05/19 | 16 : 33 : 54 | 3.2 | 36.68 | 5.25 | 9.01 | 122 | 90 | 161 | 212 | 71 | 0 | 93 | 70 |
| | | 14 | 13/05/19 | 17 : 21 : 10 | 3.0 | 36.68 | 5.26 | 9.60 | 152 | 82 | -135 | 54 | 45 | -11 | 87 | 68 |
| | | 15 | 13/05/25 | 21 : 16 : 11 | 3.3 | 36.69 | 5.25 | 9.81 | 116 | 86 | 145 | 209 | 45 | 3 | 100 | 71 |
| | | 16 | 13/05/26 | 16 : 00 : 55 | 5.0 | 36.68 | 5.25 | 9.51 | 137 | 73 | -168 | 44 | 79 | -17 | 100 | 73 |
| | | 17 | 13/05/26 | 16 : 51 : 59 | 3.0 | 36.68 | 5.27 | 9.93 | 155 | 87 | -138 | 62 | 48 | -4 | 100 | 79 |
| | | 18 | 13/05/26 | 16 : 53 : 06 | 3.0 | 36.69 | 5.26 | 9.93 | 127 | 72 | 157 | 224 | 70 | 19 | 100 | 71 |
| | | 19 | 13/05/26 | 17 : 16 : 25 | 3.0 | 36.68 | 5.26 | 9.65 | 135 | 85 | -138 | 40 | 49 | -7 | 90 | 72 |
| | C3-C4 | 20 | 13/05/26 | 17 : 37 : 07 | 3.0 | 36.68 | 5.26 | 9.73 | 201 | 83 | 154 | 295 | 65 | -8 | 100 | 68 |
| | | 21 | 13/05/26 | 20 : 08 : 19 | 3.0 | 36.69 | 5.26 | 9.77 | 120 | 48 | 173 | 214 | 85 | 42 | 88 | 61 |
| | | 22 | 13/05/26 | 20 : 14 : 56 | 3.3 | 36.68 | 5.26 | 9.83 | 166 | 62 | -166 | 69 | 78 | -28 | 100 | 65 |
| | | 23 | 13/05/26 | 20 : 39 : 51 | 3.0 | 36.68 | 5.26 | 9.64 | 131 | 88 | -169 | 41 | 79 | -2 | 95 | 67 |
| | | 24 | 13/05/27 | 12 : 33 : 29 | 3.3 | 36.69 | 5.26 | 9.61 | 141 | 82 | -173 | 50 | 83 | 8 | 100 | 73 |
| | | 25 | 13/05/27 | 12 : 45 : 32 | 3.2 | 36.68 | 5.26 | 9.42 | 109 | 86 | 15 | 17 | 75 | 175 | 100 | 67 |
| | | 26 | 13/05/27 | 17 : 04 : 19 | 3.5 | 36.69 | 5.26 | 9.59 | 131 | 78 | 158 | 226 | 69 | 13 | 95 | 70 |
| | | 27 | 13/05/27 | 21 : 07 : 26 | 3.0 | 36.69 | 5.26 | 9.70 | 123 | 82 | 173 | 214 | 83 | 8 | 100 | 69 |
| | | 28 | 13/05/28 | 00 : 14 : 03 | 3.1 | 36.68 | 5.26 | 9.78 | 140 | 86 | -133 | 46 | 43 | -5 | 93 | 71 |
| | | 29 | 13/05/30 | 02 : 34 : 01 | 3.1 | 36.69 | 5.26 | 9.47 | 117 | 62 | -161 | 18 | 74 | -29 | 100 | 66 |
| **The 2006-2020 Babors main events** | L | 30 | 06/03/20 | 19 : 44 : 23 | 5.6 | 36.56 | 5.41 | 7.70 | 92 | 64 | -174 | 360 | 84 | -26 | - | - |
| | | 31 | 17/03/30 | 01 : 41 : 07 | 3.3 | 36.58 | 5.21 | 10.53 | 35 | 83 | 10 | 303 | 80 | 172 | 87 | 70 |
| | | 32 | 17/07/27 | 07 : 04 : 03 | 3.5 | 36.58 | 5.21 | 7.19 | 321 | 74 | 171 | 54 | 81 | 15 | 88 | 67 |
| | TZNB | 33 | 18/02/06 | 14 : 27 : 23 | 4.1 | 36.60 | 5.21 | 10.80 | 32 | 66 | 12 | 297 | 78 | 155 | 86 | 71 |
| | | 34 | 18/02/09 | 15 : 34 : 49 | 3.7 | 36.59 | 5.21 | 10.09 | 38 | 83 | 8 | 307 | 81 | 173 | 86 | 77 |
| | | 35 | 19/07/14 | 12 : 55 : 39 | 3.1 | 36.56 | 5.22 | 6.89 | 296 | 78 | 176 | 26 | 86 | 11 | 84 | 67 |
| | D1 | 36 | 18/07/20 | 09 : 32 : 58 | 3.8 | 36.53 | 5.26 | 6.19 | 302 | 81 | -167 | 210 | 77 | -8.6 | 84 | 70 |
| | D2 | 37 | 20/01/17 | 17 : 53 : 18 | 3.0 | 36.54 | 5.24 | 9.30 | 57 | 75 | 6 | 325 | 84 | 165 | 100 | 70 |
| | A1 | 38 | 18/08/19 | 12 : 20 : 03 | 4.2 | 36.63 | 5.28 | 9.90 | 171 | 87 | 11 | 80 | 78 | 177 | 100 | 67 |
| | A2 | 39 | 20/01/15 | 17 : 57 : 25 | 3.0 | 36.60 | 5.29 | 8.90 | 36 | 72 | -12 | 130 | 77 | -162 | 100 | 74 |
| | B | 40 | 20/01/07 | 08 : 31 : 51 | 3.0 | 36.78 | 5.24 | 4.20 | 131 | 75 | •-174 | 40 | 84 | -14 | 100 | 72 |

'Score' and 'quality' are two parameters that measure the similarity between polarities observed and predicted by the model. C1: Cluster 1; C2: Cluster 2; C3–C4: Clusters 3 and 4; L: Lâalam earthquake; TZNB: 2017–2020 Tizi N'Berber events; D1: Darguinah event 1; D2: Darguinah event 2; A1: Aokas event 1; A2: Aokas event 2; B: 2020 Bejaia event

the lateral distribution of seismic events. The mean fault dip is ∼ 78°.

Cross-sections *A–A′*, *B–B′*, *C–C′*, and *D–D′* (Fig. 6c) indicate that the event foci are generally distributed on a high-angle dip fault plane, at depths of 6–12 km. Cross-section *A–A′* shows that the aftershock locations associated with cluster C1 are relatively diffuse and show no clear dip orientation.

σ1: 14/359
σ2: 74/208
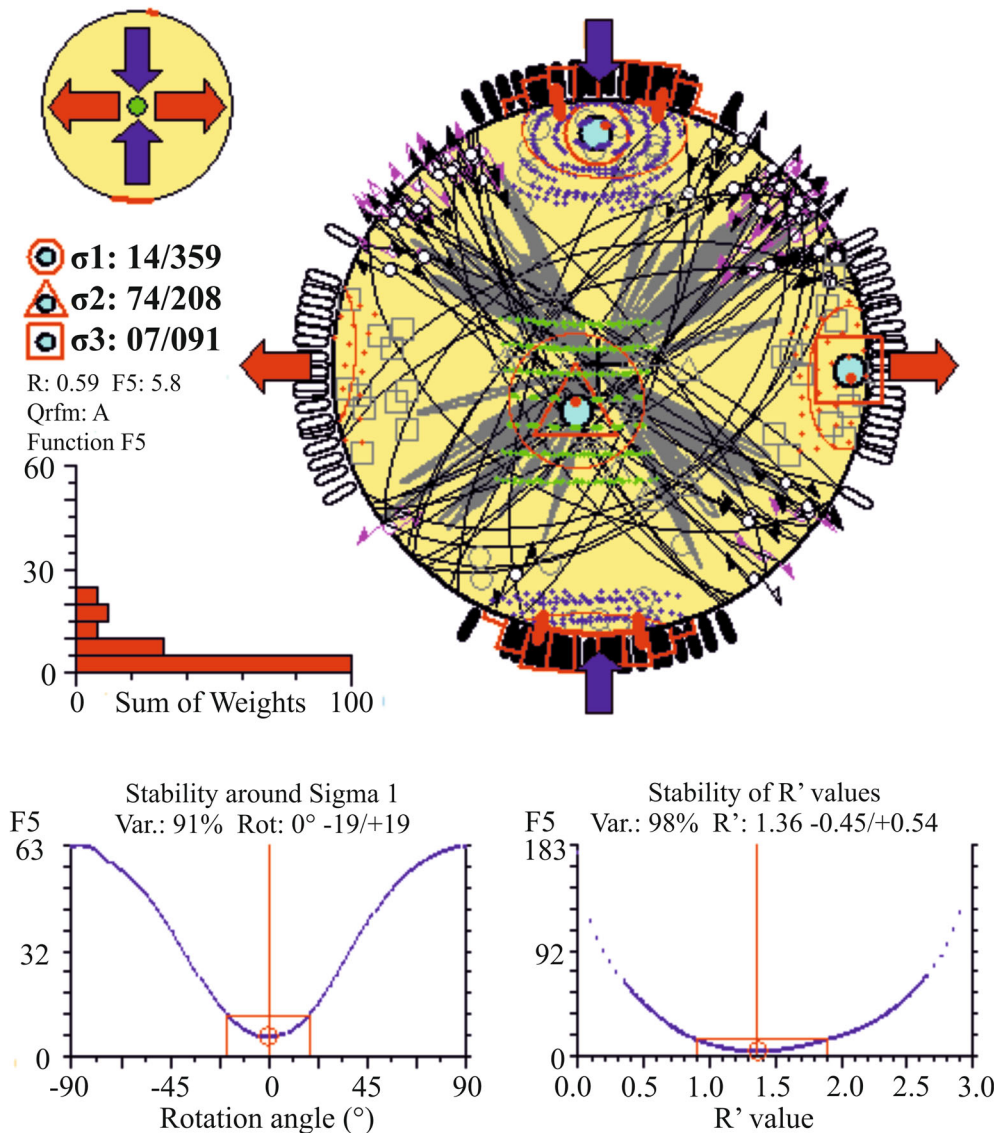σ3: 07/091

R: 0.59  F5: 5.8
Qrfm: A
Function F5

Figure 7
Stress tensor inversion result showing selected focal planes projected onto the lower hemisphere (Schmidt stereographic projections). The histogram represents the distribution of the misfit function F5, linearly weighted by event magnitudes. $\sigma_1$, $\sigma_2$, and $\sigma_3$ are the maximum, intermediate, and minimum principal stress axes, respectively. Stress symbols on the upper left corner show the horizontal stress axes ($S_{Hmax}$ and $S_{Hmin}$)

This is because this cluster is located far from any permanent station. Cross-sections *B–B′* (related to C2) and *C–C′* (related to C3 and C4) show a dip of ~ 70°, are consistent with the average dip across the fault, and calculated by focal mechanism solutions (Fig. 6b and Table 2). Finally, cross-section *D–D′*, which displays the most southeasterly events of

cluster C4, shows no clear dip angle but a weak trend towards the NE.

### 5.4. Stress Tensor Inversion and Coulomb Stress Changes

The results of stress tensor inversion are shown in Fig. 7. The selected nodal planes are moderate to
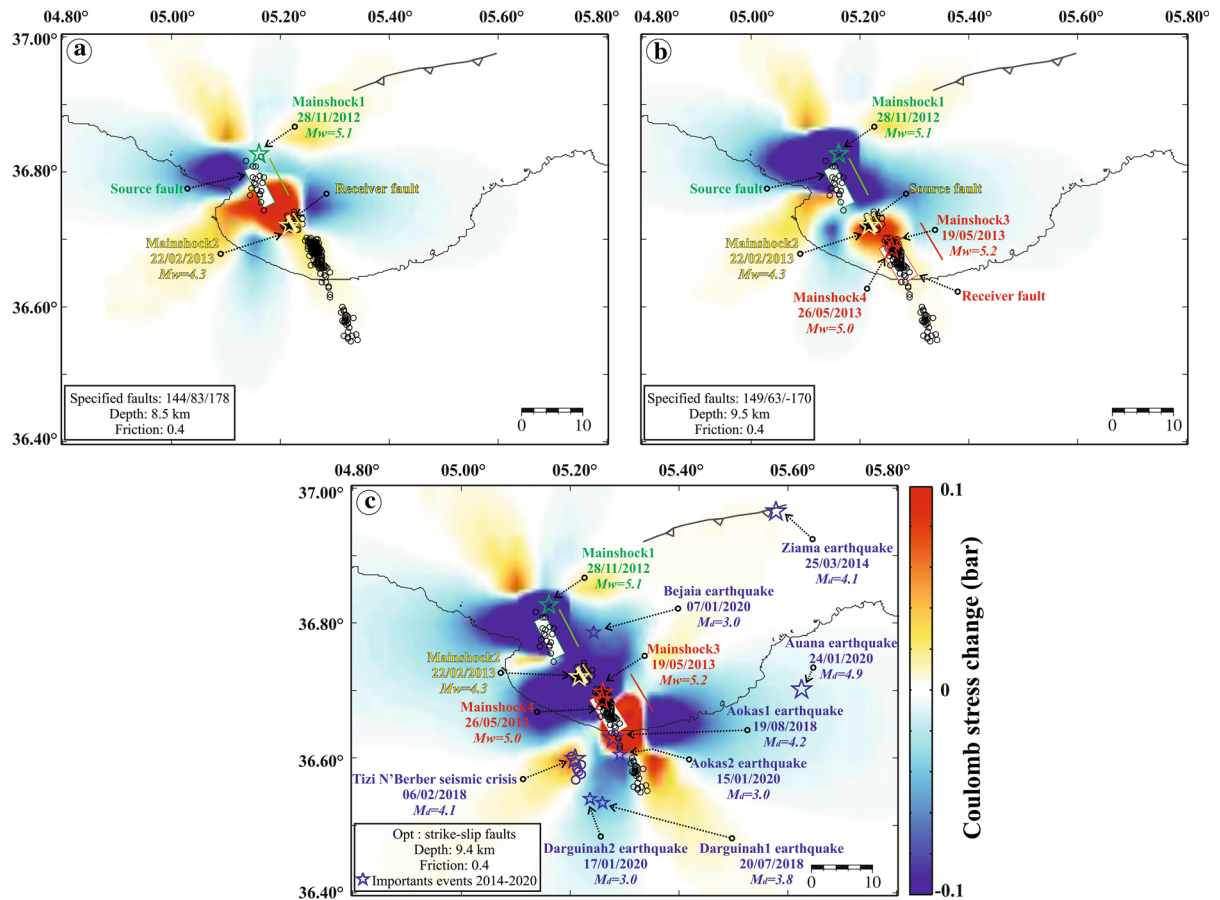
Figure 8
Coulomb stress change caused by **a** the 2012 Bejaia earthquake (Event 1) in terms of triggering the February 2013 event (Event 2), **b** Events 1 and 2 in terms of triggering the 19 May 2013 sequence (Events 3 and 4), and **c** the cumulative effect of Events 1–4 on optimally oriented fault planes. The white rectangles represent the surface faults

steeply inclined (60°–90°) and strike NW–SE and NE–SW. The steeply and shallowly dipping focal planes indicate that the maximum horizontal principal stress is oriented near N–S ($S_{Hmax} \sim \sigma_1 = N000° \pm 10.8°$). The average slip deviation is 9.9, and the quality rank "A" indicates reliable results. The computed orientations (dip/azimuth) are sub-horizontal $\sigma_1$ (14°/N359° E), near-vertical $\sigma_2$ (74°/N208° E), and sub-horizontal $\sigma_3$ (07°/N091° E) (Fig. 7). The stress regime index ($R' = 1.41 \pm 0.25$) indicates a pure strike-slip regime.

As for static stress changes, during parameterization, we tested different values of the effective friction coefficient $\mu'$, ranging from 0.2 to 0.8. Our results show that static stress changes are not strongly dependent on $\mu'$. As $\mu'$ is unknown, we set $\mu' = 0.4$, consistent with recent work on Algerian faults (Kariche et al. 2017; Khelif et al. 2018; Yelles-Chaouche et al. 2018). For each mainshock of the four sequences, we calculate the stress change on the subsequent fault segments associated with later events to better understand the link between the seismic sequences. Hereafter, we refer to the mainshocks as Events 1, 2, 3, and 4, consistent with the order in which they occurred. Fault plane geometries are obtained from the focal mechanism solutions of the specified (both source and receiver) events and the spatial distribution of aftershocks for each cluster.
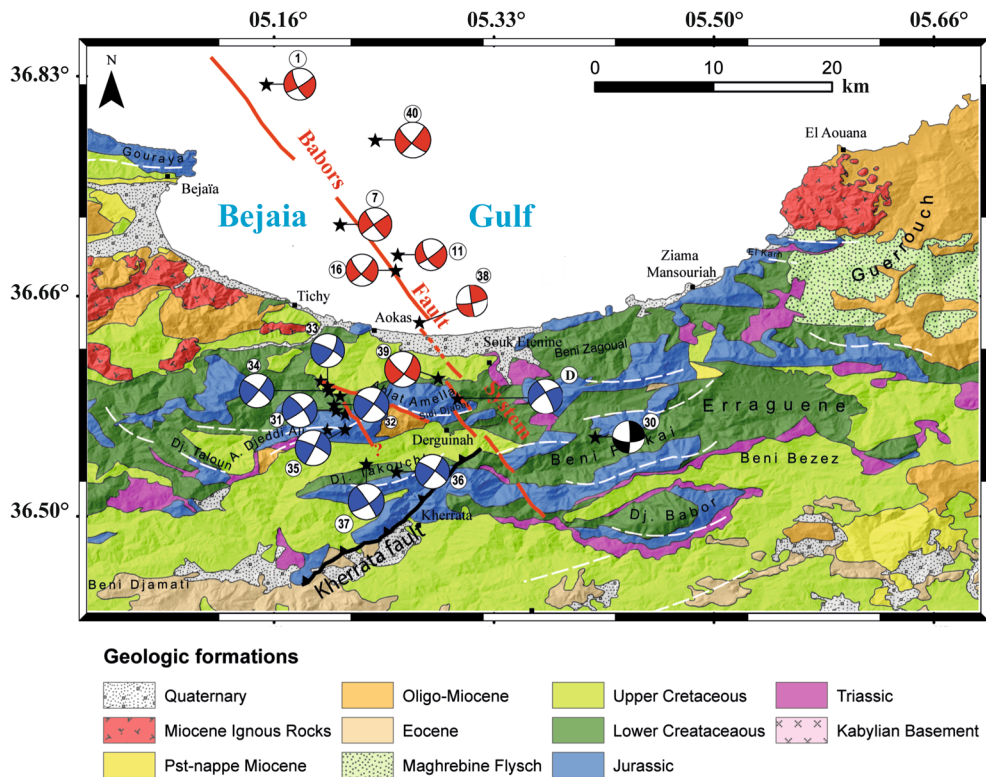
Figure 9

Geological map showing the main stratigraphic units in the Babors chain (modified and simplified from the 1:50,000 geologic map of Ziama-Mansouriah, Kireche 1993; Vila 1980). Fold axes are shown as white dashed lines (Kireche, 1993). The numbers relate to the main events that have occurred in the area since 2006, as listed in Table 2. The red lines map the lineaments associated with the BTF and TZNB-DF faults, as interpreted in this study, and the black line indicates the Kherrata Fault as mapped by Rothé (1950). Focal mechanism (D) represents that of the 1974 Darghuinah earthquake

Figure 8a shows Coulomb stress changes produced by slip associated with Event 1, at 8.5 km depth, on planes with the same orientation as the Event 2 fault plane. In the figure, the extent of the fault surface associated with Event 2 is superimposed on the stress field. We observe that Event 2 occurred in the SE of the increased Coulomb stress zone and that most of the aftershocks are associated with positive Coulomb stress changes that act to trigger failure.

Figure 8b shows the Coulomb stress change caused by slips associated with both Event 1 and Event 2, at 9.5 km depth, on planes with the same orientation as Event 3 and Event 4 (which are interpreted to have occurred on the same fault segment) fault plane. This figure shows that the previous slips of Event 1 and 2 increased the

Coulomb stress further in the SE, where Events 3 and 4 were located. This explains the SE migration of seismicity and suggests that Events 3 and 4 were triggered by slip on previously activated fault segments.

Finally, we compute the static stress change on optimally oriented fault planes that results from the slip associated with the mainshocks of all four sequences. This approach does not require consideration of the orientation of receiver faults. To compute the optimal plane, we use the three principal stress axes calculated above. As focal mechanisms of both mainshocks and aftershocks indicate strike-slip motion, the static stress change is computed on optimally oriented strike-slip planes. Figure 8c shows the cumulative static Coulomb stress change due to events 1–4 on optimally oriented fault planes at 9.4-
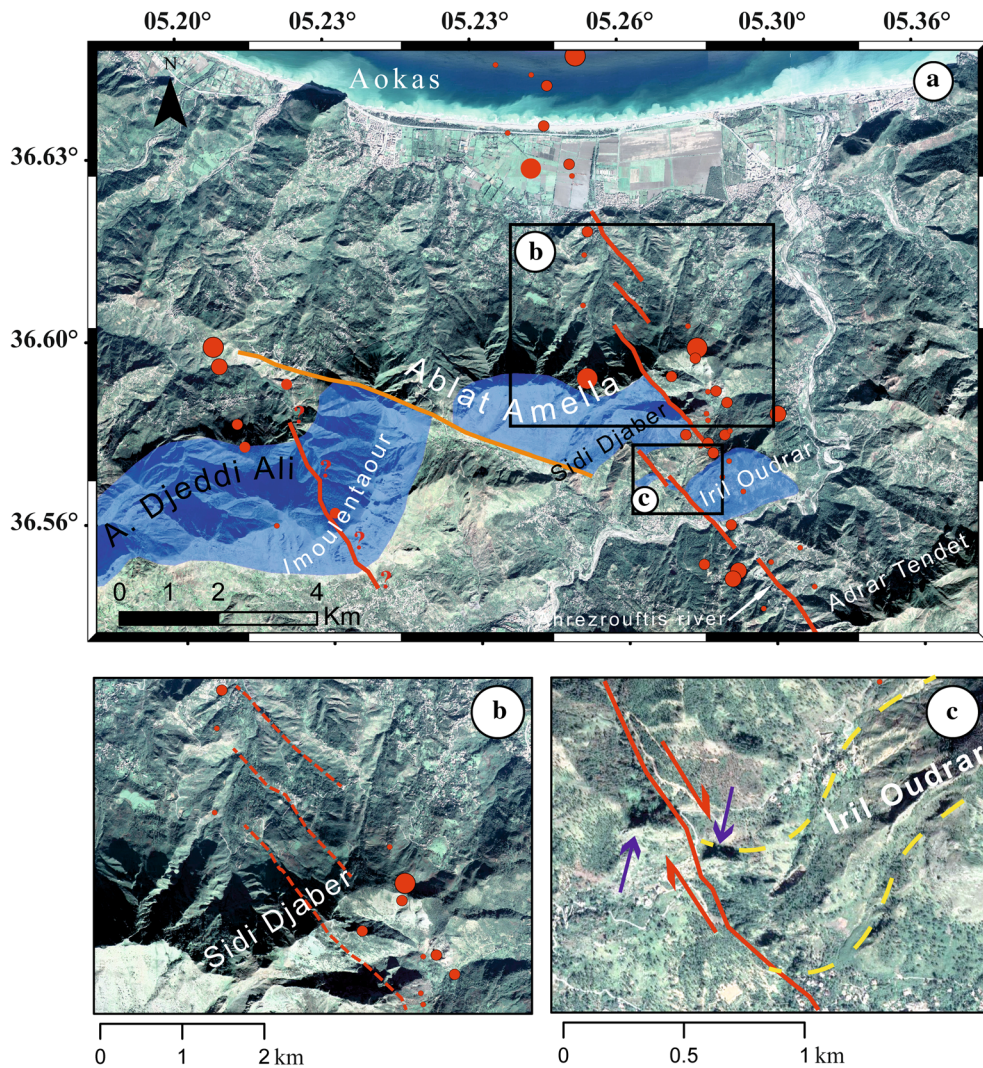
Figure 10

High-resolution Google Earth photographs showing the epicentral area of the Bejaia 2012–2013 fourth seismic sequence and the 2017–2020 Tizi N'Berber–Darguinah seismic events. Red dots indicate onshore seismic events. **a** A regional view that shows the main faults in this area. Red lines are the potentially active fault segments deduced from this study. The orange line indicates a fault that trends WNW–ESE and cuts the Jurassic massifs. **b** Enlargement showing the eastern margin of the Sidi Djeber massif, as delimited by NNW–SSE lineaments. **c** Enlargement showing the western margin of the Iril Oudrar massif and the suspected lineament of a section of the BTF in this area. Drag folding (yellow dashed lines) and clear offsets are observed associated with dextral fault movement (blue arrows)

km depth. A zone of positive Coulomb stress change occurs as a lobe-like feature that extends from the lateral location of Event 4 towards the SE corner of the seismogenic volume. The late aftershock activity associated with cluster C4 is located on the lobes of this structure. Figure 8c also shows that the epicenters of the recent $M_d$ 4.2 Aokas 1 (19 August 2018) and $M_d$ 3.0 Aokas 2 (15 January 2020) earthquakes

are located over this structure. Positive Coulomb stress changes also occur on a parallel (NW–SE-trending) structure where several recent earthquakes, such as where the Tizi N'Berber earthquake (6 February 2018) was located.

Spatiotemporal distribution of earthquakes revealed NW–SE hypocentral migration from the starting point, suggesting the division of the seismic
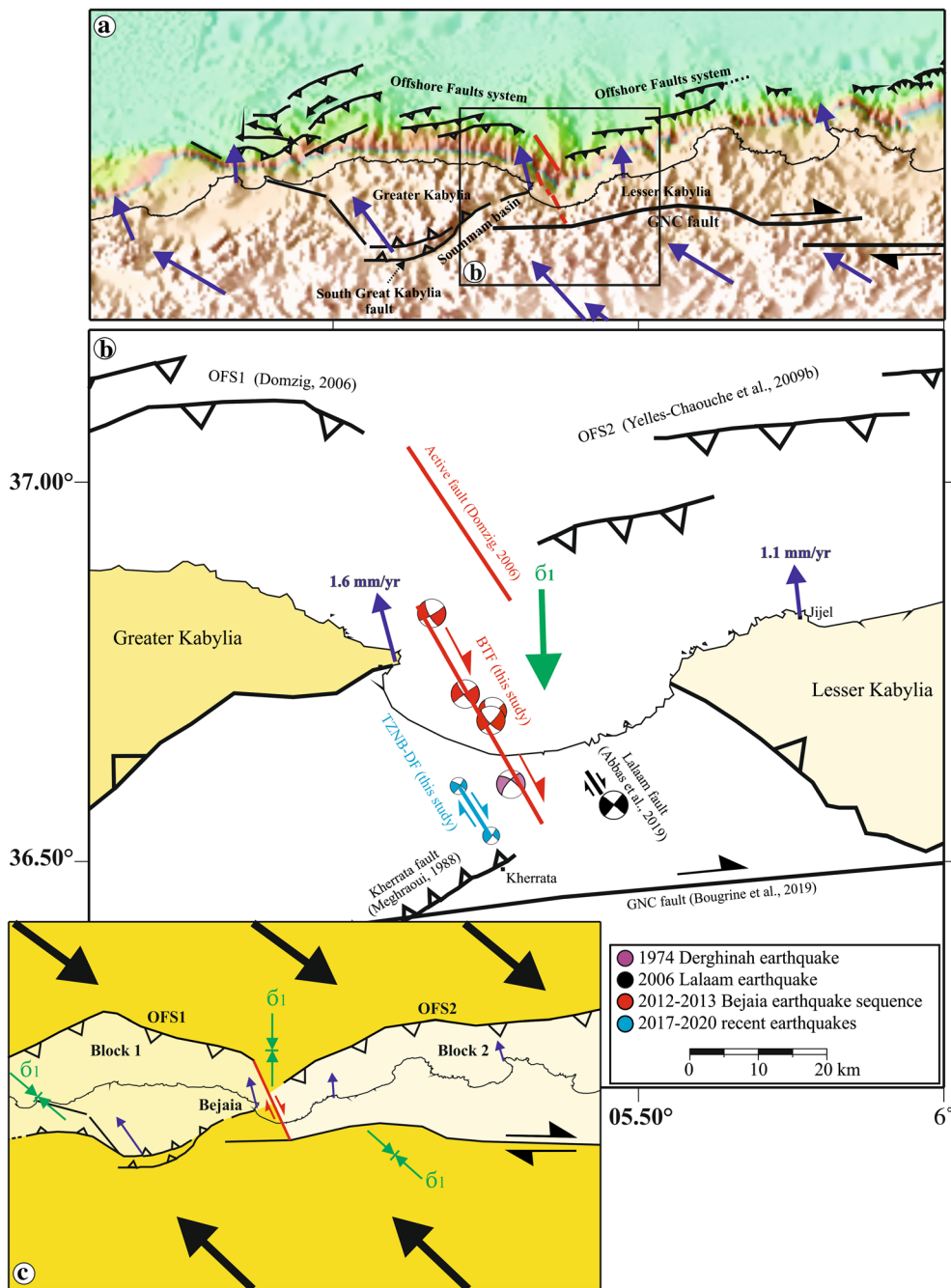
Figure 11

**a** Map showing the various fault systems located in the study area: (1) the Offshore Fault System (OFS), adapted from Domzig (2006), Yelles-Chaouche et al. (2009b), and Kherroubi et al. (2009); (2) the E–W-striking, right-lateral Ghardimaou–North Constantine (GNC) Fault (Bougrine et al. 2019; Meghraoui & Pondrelli 2012); and (3) the south Greater Kabylia faults (Boudiaf 1996). GPS velocities are shown relative to Eurasia (Bougrine et al. 2019). **b** Map showing the location of the study area in the transfer zone between the OFS and the N–W-striking dextral GNC Fault. Established composite solution (black) of fault mechanisms from seven aftershocks of the 2006 Lâalam earthquake in Abbes et al. (2019) which reveals right-lateral strike-slip faulting. **c** Modeled transfer fault (BTF + TZNB-DF + Lalaam fault + NNW–SSE offshore active fault) in a regional context. GPS velocities are shown relative to the Eurasia plate (purple arrows)

sequence into five of four major clusters. The hypocentral migration was corroborated by the Coulomb stress change calculation, indicating that four fault segments involved in the rupture process successfully failed due to static stress transfers.

## 6. Relation to Local-Scale Geology

Based on the distribution of aftershock locations and focal mechanism solutions, we attempt to infer the relationship between the local geology and the Bejaia earthquake sequences. The lack of recent sedimentary deposits means that it is difficult to identify potentially active faults by neotectonic analysis. The 2012–2013 events occurred in four clusters that define a NW–SE-trending linear structure, extending from the Gulf of Bejaia to the central part of the Babors mountain range. Although limited sub-bottom data have been collected in the gulf, we used data from previous works (Domzig 2006; Harbi et al. 1999) to constrain the location of the fault lineament at sea. Onshore, where the events are distributed between the settlements of Aokas and Derguinah, a geological structure can be identified using remote sensing techniques, geomorphic analysis (based on digital elevation models), and data from previous geological studies (Kireche 1993). The structure revealed by these methods defines a fault system that matches both the spatial distribution of aftershocks and one of the nodal planes of the focal mechanism solutions (Fig. 9). The SE part of cluster zone C4, located SE of Aokas, is affected by a fault system that strikes 145° and cuts belts of folded Jurassic limestone. Figure 10 shows a high-resolution photograph of the area associated with cluster C4. Many indicators of dextral strike-slip movement are observed. Figure 10c shows drag folds and stratigraphic offsets consistent with dextral strike-slip movement along the fault that marks the western border of the Iril Oudrar massif. A few kilometers to the west, at the Tizi N'Berber–Derguinah area, we observe a fault striking 115° (orange fault in Fig. 10a) that cuts the Jurassic blocks of the Ablat Amella and Imoulentaour massifs. Cumulative dextral offsets of up to 1 km are observed along this fault (Fig. 10a). However, in the epicentral area of the

2017–2020 Tizi N'Berber–Darguinah event, which consists of a cluster of 11 events ($M_d \geq 3.0$) precisely relocated in this study (Figs. 8c, 9 and Table 2), their distributions show a fault segment located 10 km west of the BTF, oriented NW–SE on a right-lateral strike-slip fault. Previously unknown, we name it the Tizi N'Berber–Darguinah Fault (TZNB-DF) (Fig. 11b). These events are not aligned with the 115° striking lineament but map onto a lineament that runs parallel to the fault system striking 145° (i.e., the red fault marked with "?" in Figs. 9 and 10a). This fault is not evident on satellite images, suggesting that it may be a blind fault. In making these observations, we did not evaluate the active tectonics affecting Plio-Quaternary formations, as this is beyond the scope of this study. The location and focal mechanisms of seismicity in this area suggest that activity results from the reactivation of preexisting faults that formed during previous polyphase deformation, in response to changes in the local stress regime.

## 7. Discussion

Our study used the opportunity provided by the seismic sequences that occurred between 2012 and 2013 and backed by good-quality data for recent moderate events recorded until 2020 to explore a seismotectonically poorly known region.

Although the 2012–2013 Babors–Bejaia seismic sequences released moderate events, the recognition of the related seismogenic fault pattern is particularly relevant in light of defining a new seismotectonic model useful to give new insights on the kinematics and the structural style of the active deformation in this undiscovered area, known for its complex active tectonics by connecting several seismogenic zones; the Soummam basin, the two paleozoic Kabylia blocks, Offshore Fault System (OFS) north, and GNC fault south (Fig. 11a).

From this study, the newly discovered BTF and TZNB-DF are NNW–SSE-striking, dextral strike-slip faults which, in combination with the NNW–SSE offshore active fault (Domzig, 2006) and the Lâalam fault (Abbes et al. 2019), define a new dextral transfer zone which involves several sub-crustal fault segments that separate the Greater and Lesser Kabylia
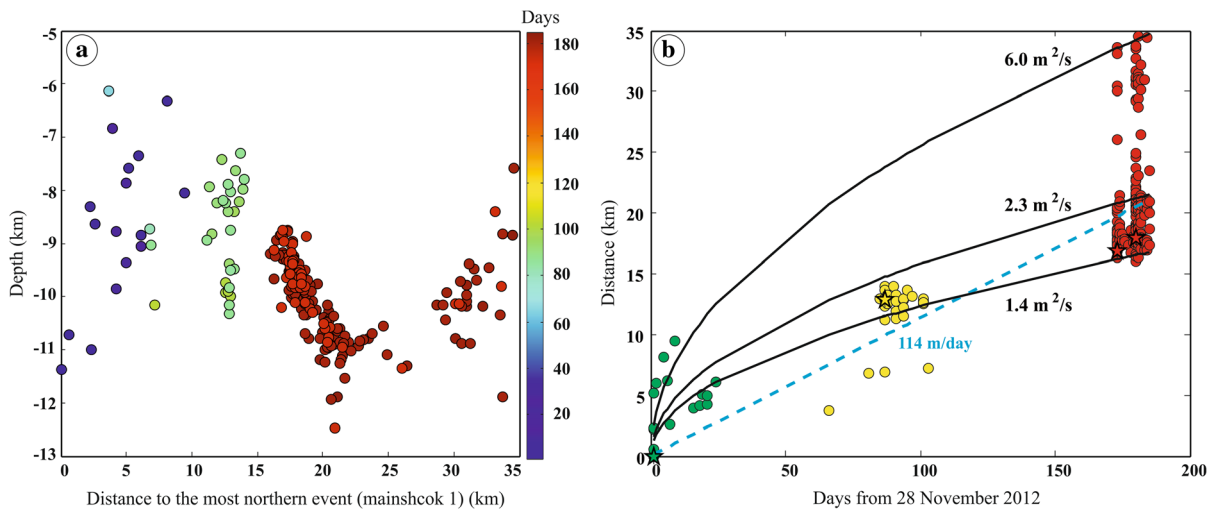
Figure 12

**a** The map shows a migration pattern. Earthquakes that belong to different clusters are denoted with different colors. **b** Hypocentral separation of events with time since the first event for the entire sequence. Thick black curves show diffusion rates of 1.4 m²/s, 2.3 m²/s, and 6 m²/s, respectively. The dashed blue line is a constant migration velocity of 144 m/day. Colored circles are earthquakes in identified clusters: C1 (green), C2 (yellow), and C3–C4 (red)

blocks. This inference is supported by also the shortening variation on the order of 0.5 mm/year between the two blocks 1 & 2 or OFS1&2 faults located on each side of the transfer zone (Fig. 11b). This transfer zone (red fault in Fig. 11c) links the E–W-striking OFS1&2 faults situated north of the two Kabylian blocks and the E–W-striking Ghardimaou–North Constantine Fault (GNC) located inland to the south, which both accommodate the shortening resulting from the oblique convergence of the African and Eurasian plates. Slip deficit rates associated with the OFS1&2 faults range from 4.4 mm/year in western Algeria to 1.5 mm/year in eastern Algeria, while the GNC fault accommodates a slip deficit rate of 2.4 mm/year (Bougrine et al. 2019).

From the stress field issue, the stress field can be deflected into sub-parallel or sub-perpendicular orientations regarding the pre-existing faults (Tingay et al. 2010), or stress rotation can occur within broad, active fault zones (e.g., Townend & Zoback 2004); these changes are known from geomechanical studies. Along the Babors–Bejaia zone, the first-order $S_{Hmax}$ orientation relatively consistent with the relative plate motion of Africa–Eurasia highlights the role of large tectonic forces in a first-order stress pattern (Heidbach et al. 2016). The first-order stress

field in the Babors–Bejaia region is largely a consequence of compressional forces at the Africa–Eurasia plate boundary, primarily relating to ridge push and continental collision (Meghraoui & Pondrelli 2012; Nocquet 2012). This is illustrated by Beldjoudi et al.'s (2009) estimate of a NW–SE-trending maximum principal stress axis in the Babors mountain range, based on an analysis of the 2006 Lâalam earthquake and regional focal solutions (Fig. 2b), in agreement with the regional velocity field (Bougrine et al. 2019). Besides, the local $S_{Hmax}$ (N180° E) orientation found by our analysis follows the local velocity field at Bejaia city (N171° E) (Bougrine et al. 2019), not parallel to both (N134° E) stress direction and (N131° E) velocity direction at regional scales, which reinforces the moderate clockwise rotation (46°) for stress and (40°) for velocity around the Babors Transverse Fault shear zone revealed in this study. Therefore, the dominant N–S right-lateral shear deformation associated with an average E–W extension (Fig. 7 upper left) makes the Babors–Bejaia domain to play a pivotal role by accommodating parts of slip, on strike-slip structure parallel to the oblique convergent plates and also involved in the reorientation of the stress field. At a large scale, the interpreted present-day $S_{Hmax}$ runs NW–SE to N–S, interrupted by

local perturbations, suggesting that plate-driving forces related to the Africa–Europe convergence impose the largest component of the total stress field. In the transfer zone, the horizontal stress direction (Fig. 11c) is oriented N–S perfectly consistent with strain partitioning, with pure thrust slip along offshore faults OFS2 and pure right-lateral strike-slip along the GNC fault bounding the Lesser Kabylia block2. The GNC fault pulls the movement of the deformation in block 2 and results in variation of 0.5 mm/year between OFS1&2 of Greater and Lesser Kabylia blocks, respectively. The western tip of the GNC Fault borders the Lesser Kabylia block2 to end most likely connected to the highlighted transfer zone in the Babors region.

Figure 11 schematized the new findings obtained from this study in conjunction with previous results that describe recent deformation on several active faults in the Bejaia–Babors and Jijel regions (Yelles-Chaouche et al. 2021). This figure illustrates the role of the BTF in transferring deformation among different active structures. This structure could have played a major role in the suture of the Lesser Kabylian block to the African plate.

On the other hand, the rupture along the BTF zone supposes an earthquake-to-earthquake triggering. The seismic activity begins in the NW in segment S1 and migrates SE to segment S2, before terminating in S3 and S4. The occurrence of event migration between adjacent segments, initiated by different triggers at each segment, implies that each event occurred in a segment previously stressed by lateral Coulomb stress interactions. This suggests that the loading was in a particular state of stress (i.e., uniform and close to failure) along all fault segments, to enable propagating earthquake sequences (Pondard et al. 2007). Fault interaction, as investigated by static stress changes, showed that these "triggers" cause small variations in the static stress field (< 0.1 bar), capable of inducing the reactivation of nearby faults which are close to failure (Toda et al. 1998; Ziv & Rubin 2000). This process may induce aftershocks, or even major earthquakes, in neighboring areas (Stein 1999). The similar fault plane solutions obtained for all moderate-magnitude ($M_d \geq 3$) events suggest a uniform stress field within the seismogenic volume.

The occurrence of the Aokas 1 earthquake ($M_d = 4.2$) of 19 August 2018, which was located on the southern part of segment S3, and the Aokas 2 event ($M_d = 3.0$) of 15 January 2020, located between segments S3 and S4, suggests that the BTF is still releasing accumulated energy, as confirmed by the Coulomb stress changes. Other earthquakes have occurred on the fault in the past, such as the $M_b = 4.7$ event of 29 June 1974 (Figs. 9 and 11b), which struck the Darguinah region. This event was located on segment S4 of the BTF and showed right-lateral strike-slip movement, a NW–SE strike, and a steep dip towards the NE (Hatzfeld 1978). Therefore, a future rupture could occur over multiple adjacent segments, resulting in other moderate earthquakes.

Then, to understand the spatiotemporal evolution of the seismic sequences in the context of driving mechanics, the role of the fluids has been addressed in several previous studies (e.g., Bourouis & Cornet 2009; Chen et al. 2012; Duverger et al. 2015). Indeed, as we noticed the migration pattern in the Bejaia–Babors seismic sequences (Fig. 12a), we investigated the seismicity migration to explore if fluids are involved in the successive failures. The fluid-involved swarms can be modeled as a diffusion process, with diffusivity ranging from 0.02 to about 10 m²/s (e.g., do Nascimento 2005; Parotidis et al. 2003; Shapiro et al. 2005). To test fluid diffusion, we model seismicity using the equation of Shapiro et al. (1997) by calculating the distance $r$ of a propagating pore-pressure front diffusing at rate $D$ during time $t$ through a homogeneous isotropic saturated poroelastic medium from a point source as (Fig. 12b):

$$r = \sqrt{4\pi Dt}. \tag{2}$$

Additionally, the pore fluid diffusion is typically at velocities on the order of meters per day, generally much slower than aseismic slip-driven migration, which is usually at kilometers per hour (Roland & McGuire 2009). Figure 12b shows seismicity spreading at a similar rate to diffusion in the range of 5–6 m²/s or constant migration velocity on the order of 114 m per day. This migration rate on this order could be associated with fluid flow through a fractured volume. Then we concluded that the fluids played a role in the spatiotemporal evolution of Beajia–Babors sequences.

Several important implications for seismic hazard in the study area arise from the analysis of those

seismic sequences. The expansion of the rupture zone during 6 months shows a total subsurface rupture length of about 30 km. Therefore, a larger earthquake might be possible in this region if simultaneous rupture occurs across the four fault segments. The scaling relations of Wells and Coppersmith (1994) forecast for a strike-slip fault which has a subsurface length of 30 km, width of 12 km, and a magnitude of about $M_w = 6.5$. Since the fault is near the city of Bejaia, added to landslides which constitute a perpetual threat to people's life and goods in the Babors chain area, especially during the occurrence of an earthquake, even of moderate magnitude (Guemache et al. 2010), the seismic hazard in the region must be reassessed using a multidisciplinary approach.

## 8. Conclusion

This study focused on the most representative seismic sequences in the region of Bejaia for the last decade (2010–2020); this work investigates the 2012–2013 Bejaia seismic sequences that hit the Babors region, on the north coast of Algeria, over 6 months. The analysis of seismic sequences in the Babors has identified, for the first time, NW–SE-striking strike-slip faults that we name the Babors Transverse Fault (BTF) and the Tizi N'Berber–Darguinah Fault (TZNB-DF).

The high-precision relocation of 252 events, in conjunction with focal mechanism solutions, shows a 35-km-long, NW–SE-striking, near-vertical right-lateral strike-slip fault. The BTF extends from the Babors chain to the Gulf of Bejaia. The seismic events were grouped into four clusters (C1–C4) generated by the failure of four fault segments (S1–S4). As the total energy release was distributed over four BTF segments, a potentially higher-magnitude and more dangerous earthquake might have been avoided.

The transfer fault zone is shaped as on echelon segments faults; the BTF, TZNB-DF, the NNW–SSE offshore active fault, and the Lâalam fault connecting the offshore thrust faults system in the north and the right-lateral strike-slip GNC Fault in the south. The seismic events between 2017 and 2020 suggest that the BTF is still releasing accumulated energy, as also

indicated by Coulomb stress change analysis, and the observed migration of the seismicity also is compatible with earthquake triggering by fluid diffusion processes.

The present study highlights the BTF as a likely source for both recent and historic seismic activity in the region. Analysis of high-resolution photography indicates dextral movement along old polyphase structures, suggesting the reactivation of preexisting faults in response to the current stress regime. Finally, the study suggests that a reassessment of the seismic hazard risk for Bejaia city is necessary, as the possibility of a large-slip event on the BTF is not excluded. Further investigations are required to establish a tsunamigenic risk assessment along the Bejaia coastline for better land planning in the region.

**Publisher's Note**   Springer Nature remains neutral with regard to jurisdictional claims in published maps and institutional affiliations.

### REFERENCES

Abacha, I. (2015). Étude de la sismicité de la région Nord-Est de l'Algérie, PhD thesis, University Ferhat Abbas-Sétif, Algeria. http://dspace.univ-setif.dz:8888/jspui/handle/123456789/1802.

Abacha, I., Koulakov, I., Semmane, F., & Yelles-Chaouche, A. (2014). Seismic tomography of the area of the 2010 Beni-Ilmane earthquake sequence, north-central Algeria. *Springer Plus, 3*, 650. https://doi.org/10.1186/2193-1801-3-650.

Abacha, I., & Yelles-Chaouche, A. K. (2019). *Overview of recent seismic activity in Northeastern Algeria, on significant applications of geophysical methods.* (pp. 203–206). Berlin: Springer.

Abbes, K., Dorbath, C., Dorbath, L., et al. (2019). Revisiting the Laalam (Eastern Algeria) March 20, 2006 (Mw 5.1) earthquake and its seismotectonic implication. *Pure Applied Geophysic, 176*, 4213–4222. https://doi.org/10.1007/s00024-019-02206-3.

Aidi, C., Beslier, M. O., Yelles-Chaouche, A. K., Klingelhoefer, F., Bracene, R., Galve, A., Bounif, A., Schenini, L., Hamai, L., Schnurle, P., Djellit, H., Sage, F., Charvis, P., & Déverchère, J. (2018). Deep structure of the continental margin and basin off Great Kabylia, Algeria—New insights from wide-angle seismic data modeling and multichannel seismic interpretation. *Tectonophysics, 728*, 1–22.

Akoglu, A. M., Cakir, Z., Meghraoui, M., Belabbes, S., El Alami, S. O., Ergintav, S., & Akyüz, H. S. (2006). The 1994–2004 Al Hoceima (Morocco) earthquake sequence: Conjugate fault ruptures deduced from In-SAR. *Earth Planet Science Letter, 252*, 467–480.

Ayadi, A., Dorbath, C., Ousadou, F., Maouche, S., Chikh, M., Bounif, M. A., & Meghraoui, M. (2008). Zemmouri earthquake

rupture zone (Mw 68, Algeria): Aftershocks sequence relocation and 3D velocity model. *Journal of Geophysics Research, 113*, B09301. https://doi.org/10.1029/2007JB005257.

Beldjoudi, H., Guemache, M. A., Kherroubi, A., Semmane, F., Yelles-Chaouche, A. K., Djellit, H., Amrani, A., & Haned, A. (2009). The Laâlam (Béjaïa, North-East Algeria) moderate earthquake (Mw = 5.2) on March 20th, 2006. *Pure and Applied Geophysics, 166*, 623–640.

Bendjama, H., Yelles-Chaouche, A. K., Boulahia, O., Abacha, I., et al. (2021). The March 2017 earthquake sequence along the E–W-trending Mcid Aïcha-Debbagh Fault, northeast Algeria. *Geosciences Journal.* https://doi.org/10.1007/s12303-020-0059-y.

Bird, P. (2003). An updated digital model of plate boundaries. *Geochemistry, Geophysics, Geosystems, 4*, 1027. https://doi.org/10.1029/2001GC000252,3.

Boudiaf, M. A. (1996). *Etude sismotectonique de la région d'Alger et de la Kabylie (Algérie)*. PhD thesis, Université de Montpellier, France.

Bougrine, A., Yelles-Chaouche, A. K., & Calais, E. (2019). Active deformation in Algeria from continuous GPS measurements. *Geophysical Journal International, 217*, 572–588.

Bouhadad, Y., Nour, A., Laouami, N., & Belhai, D. (2003). The Beni-Ourtilane-Tachaouaft fault and Seismotectonic aspects of the Babors region (NE of Algeria). *Journal of Seismology, 7*, 79–88.

Bouillin, J. P. (1986). Le "bassin maghrebin"; une ancienne limite entre l'Europe et l'Afrique a l'ouest des Alpes. *Bulletin Society Géology France, II*(4), 547–558.

Bounif, A., Dorbath, C., Ayadi, A., Meghraoui, M., Beldjoudi, H., Laouami, N., Frogneux, M., Slimani, A., Alasset, P. J., Kharroubi, A., Ousadou, O., Chikh, M., Harbi, A., Larbes, S., & Maouche, S. (2004). The 21 May 2003 Zemmouri (Algeria) earthquake Mw 6.8: Relocation and aftershock sequence analysis. *Geophysics Research Letters, 31*, L19605.

Bourouis, S., & Cornet, F. H. (2009). Microseismic activity and fluid fault interactions: Some results from the Corinth Rift Laboratory (CRL), Greece. *Geophysical Journal International, 178*, 561–580.

Buforn, E., Bezzeghoud, M., Udias, A., & Pro, C. (2004). Seismic sources on the Iberia African plate boundary and their tectonic implications. *Pure Applied Geophysics, 161*, 623–646.

Buforn, E., López-Sánchez, C., Lozano, L., et al. (2020). Re-evaluation of seismic intensities and relocation of 1969 Saint Vincent Cape seismic sequence: A comparison with the 1755 Lisbon Earthquake. *Pure and Applied Geophysics, 177*, 1781–1800.

Buforn, E., Pro, C., Sanz de Galdeano, C., Cantavella, J. V., Cesca, S., Caldeira, B., Udías, A., & Mattesini, M. (2017). The 2016 south Alboran earthquake (Mw = 6.4): A reactivation of the Ibero-Maghrebian region? *Tectonophysics, 712–713*, 704–715.

Cakir, Z., Meghraoui, M., Akoglu, A. M., Jabour, N., Belabbes, S., & Ait- Brahim, L. (2006). Surface deformation associated with theMw6.4, February 24, 2004 Al Hoceima (Morocco) earthquake deduced from InSAR: Implications for the active tectonics along North Africa. *Bulletin Seismological Society America, 96*, 1–10.

Chami, A., Yelles-Chaouche, A. K., Abacha, I., Khelif, M. F. A., & Chafik, A. (2019). The 2015 Ain-Azel (East Algeria) earthquake sequence. 2nd Conference of the Arabian Journal of Geosciences (CAJG2019), November 25–28, 2019, Sousse, Tunisia. ID 463. https://cajg.org/source/files/Program_CAJG.pdf.

Chen, X., Shearer, P. M., & Abercrombie, R. E. (2012). Spatial migration of earthquakes within seismic clusters in Southern California: Evidence for fluid diffusion. *Journal of Geophysics Research.* https://doi.org/10.1029/2011JB008973.

Cooke, M., Toeneboehn, K., & Hatch, J. (2020). Onset of slip partitioning under oblique convergence within scaled physical experiments. *Geosphere.* https://doi.org/10.1130/GES02179.1.

Delvaux, D. (2012). Release of program Win-Tensor 4.0 for tectonic stress inversion: Statistical expression of stress parameters, EGU General Assembly, Vienna, 2012. Geophysical Research Abstracts, 14, EGU2012–EGU5899.

Delvaux, D., Moeys, R., Stapel, G., Petit, C., Levi, K., Miroshnichenko, A., Ruzhich, V., & San'kov, V. (1997). Paleostress reconstructions and geodynamics of the Baikal region, central Asia, Part 2. Cenozoic rifting. *Tectonophysics, 282*(1), 1–38.

Delvaux, D., & Sperner, B. (2003). New aspects of tectonic stress inversion with reference to the TENSOR program. *Geological Society, London, Special Publications, 212*, 75–100.

do Nascimento, A. F., Lunn, R. J., & Cowie, P. A. (2005). Numerical modelling of pore-pressure diffusion in a reservoir-induced seismicity site in northeast Brazil. *Geophysical Journal International, 160*, 249–262.

Domzig, A. (2006). *Déformation active et récente, et structuration tectonosédimentaire de la marge sous-marine algérienne*. PhD thesis, Brest. Univ. Brittany, France.

Durand-Delga, M. (1969). Mise au point sur la structure du Nord-Est de la Berbérie. *Publication Service Géology Algérie, 39*, 89–131.

Duverger, C., Godano, M., Bernard, P., Lyon-Caen, H., & Lambotte, S. (2015). The 2003–2004 seismic swarm in the western Corinth rift: Evidence for a multiscale pore pressure diffusion process along a permeable fault system. *Geophysical Research Letters, 42*, 7374–7382. https://doi.org/10.1002/2015GL065298.

Gabert, P. (1984). Séismes, néotectonique et effets induits sur les versants des massifs des Babors dans la région de Kerrata (Algérie). In *Méditerranée, troisième série, tome 51, 1–2–1984. Actes du colloque «Effets des séismes sur les reliefs de forte énergie»* (pp. 25–31).

Guemache, M. A., Machane, D., Beldjoudi, H., et al. (2010). On a damaging earthquake-induced landslide in the Algerian Alps: the March 20, 2006 Laâlam landslide (Babors chain, northeast Algeria), triggered by the Kherrata earthquake (M w = 5.3). *Natural Hazards, 54*, 273–288. https://doi.org/10.1007/s11069-009-9467-z.

Guidoboni, E. (1994). *Catalogue of ancient earthquakes in the Mediterranean area up to the 10th century*. (p. 504). Instituto Nazionale di Geofisica Press.

Guiraud, R. (1977). Sur la néotectonique des régions ouest-constantinoises. *Bulletin Society Géology Fr XIX, 3*, 646–650.

Hamai, L., Petit, C., Abtout, A., Yelles-Chaouche, A. K., & Déverchère, J. (2015). Flexural behaviour of the north Algerian margin and tectonic implications. *Geophysics Journal o International, 201*, 1426–1436. https://doi.org/10.1093/gji/ggv098.

Hamai, L., Petit, C., Le Pourhiet, L., Yelles-Chaouche, A. K., Déverchère, J., Beslier, M.-O., & Abtout, A. (2018). Towards subduction inception along the inverted North African margin of Algeria? Insights from thermo-mechanical models. *Earth and Planetary Science Letters, 501*(2018), 13–23. https://doi.org/10.1016/j.epsl.2018.08.028.

Harbi, A., Maouch, S., & Benhallou, H. (2003). Re-appraisal of seismicity and seismotectonics in the north-eastern Algeria Part

II: 20th-century seismicity and seismotectonics analysis. *Journal of Seismology, 7*, 221–234.

Harbi, A., Maouche, S., & Ayadi, A. (1999). Neotectonics and associate seismicity in the Eastern Tellian Atlas of Algeria. *Journal of Seismology, 3*, 95–104.

Hatzfeld, D. (1978). *Etude sismotectonique de la zone de collision Ibéro-Maghrébine*. PhD thesis, Univ. Scie. Médi., Grenoble, France.

Hauksson, E., & Shearer, P. (2005). Southern California hypocenter relocation with waveform cross-correlation, part 1: Results using the double-difference method. *Bulletin of the Seismological Society America, 95*, 896–903.

Heidbach, O., Rajabi, M., Reiter, K., Ziegler, M., & Team, W.S.M. (2016). World Stress Map Database Release 2016, V. 1. 1., GFZ Data Services.

Kariche, J., Meghraoui, M., Ayadi, A., & Boughacha, M. S. (2017). Stress change and fault interaction from a two century long earthquake sequence in the Central Tell Atlas, Algeria. *Bulletin of the Seismological Society of America, 107*, 2624–2635.

Khelif, M. F., Yelles-Chaouche, A. K., Benaissa, Z., Semmane, F., Beldjoudi, H., Haned, A., Issaadi, A., Chami, A., Chimouni, R., Harbi, A., Maouche, S., Dabbouz, G., Aidi, C., & Kherroubi, A. (2018). The 2016 Mihoub (north-central Algeria) earthquake sequence: Seismological and tectonic aspects. *Tectonophysics, 736*, 62–74.

Kherroubi, A., Déverchère, J., Yelles-Chaouche, A. K., De-Lepinay, B. M., Domzig, A., Cattaneo, A., Bracene, R., Gaullier, V., & Graindorge, D. (2009). Recent and active deformation pattern off the easternmost Algerian margin, western Mediterranean Sea: New evidence for contractional tectonic reactivation. *Marine Geology, 261*, 17–32.

Kireche, O. (1993). *Evolution géodynamique de la marge tellienne des maghrébides d'après l'étude du domaine parautochtone schistosé (Massifs du Chélif et d'Oranie, de Blida –Bou Maad, des Babors et des Biban)*. PhD thesis, USTHB, Algeria.

Kissling, E., Ellsworth, W. L., Eberhart, P. D., & Kradolfer, U. (1994). Initial reference model in local earthquake tomography. *Journal of Geophysical Research, 99*, 19635–19646.

Kisslinger, C., & Jones, L. M. (1991). Properties of aftershock sequences in southern California. *Journal of Geophysical Research, 96*, 11947–11958.

Klein, F. (2002). User's guide to HYPOINVERSE-2000, a Fortran program to solve for earthquake locations and magnitudes. USGS Open-File Report 02–171, vers. 1, p 123.

Kohketsu, K. (1985). The extended reflectivity method for synthetic near field seismograms. *Journal of Physics of the Earth, 33*, 121–131.

Leikine, M. (1971). *Etude géologique des Babors occidentaux (Algérie)*. (p. 536). Université de Paris.

Lin, J., Stein, R.S., Meghraoui, M., Toda, S., Ayadi, A., Dorbath, C., & Belabbes, S. (2011). Stress transfer among en echelon and opposing thrusts and tear faults: Triggering caused by the 2003 Mw= 6.9 Zemmouri, Algeria, earthquake. *Journal of Geophysics Research Solid Earth 116*.

Meghraoui, M. (1988). *Géologie des zones sismiques du nord de l'Algérie (paléosismologie, Tectonique active et synthèse sismotectonique)*. PhD thesis, Univ. Paris sud Orsay, France.

Meghraoui, M., Maouche, S., Chemaa, B., Cakir, Z., Aoudia, A., Harbi, A., Alasset, P. J., Ayadi, A., Bouhadad, Y., & Benhamouda, F. (2004). Coastal uplift and thrust faulting associated with the Mw = 68 Zemmouri (Algeria) earthquake of 21 May,

2003. *Geophysics Research Letters, 31*, L19605. https://doi.org/10.1029/2004GL020466.

Meghraoui, M., & Pondrelli, S. (2012). Active faulting and transpression tectonics along the plate boundary in North Africa. *Annales Geophysicae, 55*, 955–967.

Mihoubi, A., Schnürle, P., Benaissa, Z., Badsi, M., Bracene, R., Djelit, H., Geli, L., Sage, F., Agoudjil, A., & Klingelhoefer, F. (2014). Seismic imaging of the eastern Algerian margin off Jijel: Integrating wide-angle seismic modeling and multichannel seismic pre-stack depth migration. *Geophysical Journal International, 198*, 1486–1503.

Nocquet, J. (2012). Present-day kinematics of the Mediterranean: A comprehensive overview of GPS results. *Tectonophysics, 579*, 220–242.

Nocquet, J. M., Willis, P., & Garcia, S. (2006). Plate kinematics of Nubia-Somalia using a combined DORIS and GPS solution. *Journal of Geodesy, 80*, 591–607. https://doi.org/10.1007/s00190-006-0078-0.

Ouyed, M., Meghraoui, M., Cisternas, A., Deschamps, A., Dorel, J., Frechet, J., Gaulon, R., Hatzfeld, D., & Phillip, H. (1981). Seismotectonics of El Asnam earthquake. *Nature, 292*(5818), 26–31.

Papazachos, B. C. (1975). On certain aftershock and foreshock parameters in the area of Greece. *Annali di Geofisica, 28*, 497–515.

Parotidis, M., Rothert, E., & Shapiro, S. A. (2003). Pore-pressure diffusion: A possible triggering mechanism for the earthquake swarms 2000 in Vogtland/NW-Bohemia, central Europe. *Geophysics Research Letters*. https://doi.org/10.1029/2003GL018110.

Philip, H., & Meghraoui, M. (1983). Structural analysis and interpretation of the surface deformations of the El Asnam Earthquake of October 10, 1980. *Tectonics, 2*(1), 17–49. https://doi.org/10.1029/TC002i001p00017.

Pondard, N., Armijo, R., Geoffrey, C., King, P., Meyer, B., & Flerit, F. (2007). Fault interactions in the Sea of Marmara pull-apart (North Anatolian Fault): Earthquake clustering and propagating earthquake sequences. *Geophysical Journal International, 171*, 1185–1197.

Rivera, L., & Cisternas, A. (1990). Stress tensor and fault plane solutions for a population of earthquakes. *Bulletin of the Seismological Society of America, 80*(3), 600–614.

Roland, E., & McGuire, J. (2009). Earthquake swarms on transform faults. *Geophysical Journal International, 178*, 1677–1690.

Rothé, J. P. (1950). Les séismes de Kherrata et la séismicité de l'Algérie, Bull. Serv. Cart. Geol. Algérie, 4 ème série, Géophysique, N. 3.

Scholz, C. H. (2002). *Mechanics of earthquakes and faulting*. . Cambridge University Press.

Semmane, F., Abacha, I., Yelles-Chaouche, A. K., Haned, A., Beldjoudi, H., & Amrani, A. (2012). The earthquake swarm of December 2007 in the Mila region of northeastern Algeria. *Journal of National Hazards, 64*, 1855–1871.

Serpelloni, E., Vannucci, G., Pondrelli, S., Argnani, A., Casula, G., Anzidei, M., Baldi, P., & Gasperini, P. (2007). Kinematics of the Western Africa-Eurasia plate boundary from focal mechanisms and GPS data. *Geophysical Journal International, 169*, 1180–1200.

Shapiro, S. A., Huenges, E., & Borm, G. (1997). Estimating the permeability from fluid-injection-induced seismic emissions at the KTB site. *Geophysical Journal International, 131*, F15–F18.

Shapiro, S. A., Rentsch, S., & Rothert, E. (2005). Characterization of hydraulic properties of rocks using probability of fluid-induced microearthquakes. *Geophysics, 70*, F27–F34.

Soumaya, A., Ben-Ayed, N., Rajabi, M., Meghraoui, M., et al. (2018). Active faulting geometry and stress pattern near complex strike-slip systems along the Maghreb region: Constraints on active convergence in the western Mediterranean. *Tectonics, 37*, 3148–3173.

Spakman, W., & Wortel, M. J. R. (2004). A tomographic view on western mediterranean geodynamics. In: W. Cavazza, F. Roure, W. Spakman, G. M. Stampfli, & P. Ziegler (Eds.) *The TRANSMED Atlas, The Mediterranean Region from Crust to Mantle* (Springer, Berlin, pp. 31–52). https://doi.org/10.1007/978-3-642-18919-7_2.

Stanton-Yonge, A., Griffith, W. A., Cembrano, J., Julien, R. S., & Iturrieta, P. (2016). Tectonic role of margin-parallel and margin-transverse faults during oblique subduction in the Southern Volcanic Zone of the Andes: Insights from Boundary Element Modeling. *Tectonics, 35*(9), 1990–2013.

Stein, R. S. (1999). The role of stress transfer in earthquake occurrence. *Nature, 402*, 605–609.

Stein, R. S., King, G. C. P., & Lin, J. (1992). Change in failure stress on the southern San Andreas fault system caused by the 1992 magnitude = 7.4 Landers earthquake. *Science, 258*, 1328–1332.

Strzerzynski, P., Déverchère, J., Cattaneo, A., Domzig, A., & Yelles-Chaouche, A. K. (2010). Tectonic inheritance and Pliocene-Pleistocene inversion of the Algerian margin around Algiers: Insights from multibeam and seismic reflection data. *Tectonics*. https://doi.org/10.1029/2009TC002547.

Tahayt, A., Feigl, K. L., Mourabit, T., Rigo, A., Reilinger, R., McClusky, S., et al. (2009). The Al Hoceima (Morocco) earthquake of 24 February (2004) analysis and interpretation of data from ENVISAT ASAR and SPOT5 validated by ground-based observations. *Remote Sensing of Environment, 113*(2), 306–316. https://doi.org/10.1016/j.rse.2008.09.015.

Tingay, M. R. P., Morley, C. K., Hillis, R. R., Meyer, J. (2010). Present-day stress orientation in Thailand's basins. *Journal of Structural Geology, 32*(2),235–248. https://doi.org/10.1016/j.jsg.2009.11.008.

Toda, S., Stein, R. S., Reasenberg, P. A., Dieterich, J. H., & Yoshida, A. (1998). Stress transfers by the 1995 Mw = 6.9 Kobe, Japan, shock: Effect on aftershocks and future earthquake probabilities. *Journal of Geophysical Research, 103*, 24543–24566.

Townend, J., & Zoback, M. D. (2004). Regional tectonic stress near the San Andreas Fault in central and southern California. *Geophysical Research Letters, 31*, L15S11. https://doi.org/10.1029/2003GL018918.

Udias, A., & Buforn, E. (1994). Seismotectonics of the Mediterranean region. *Advances in Geophysics., 36*, 121–209. https://doi.org/10.1016/S0065-2687(08)60538-5.

Utsu, T. (1961). A statistical study on the occurrence of aftershocks. *Geophysical Magazine, 30*, 521–605.

Utsu, T. (1969). Aftershocks and earthquake statistics (I)-Some parameters which characterize an aftershock sequence and their interrelation. *Journal of Faculty Science Hokkaido University Series VII, 2*, 129–195.

Utsu, T. (2002). *Statistical features of seismicity, international handbook of earthquake and engineering seismology*. (Vol. 81a, pp. 719–732). Elsevier.

Utsu, T., & Ogata, Y. (1995). The centenary of the Omori formula for a decay law of aftershock activity. *Journal of Physics of the Earth, 43*(1), 1–33.

Vila, J. M. (1980). *La chaîne alpine d'Algérie orientale et des confins algéro-tunisiens*. PhD thesis, Univ. Pierre Marie Curie Paris-VI, France.

Waldhauser, F., & Ellsworth, W. L. (2000). A double-difference earthquake location algorithm: Method and application to the northern Hayward fault, California. *Bulletin of the Seismological Society of America, 90*, 1353–1368.

Waldhauser, F., & Schaff, D. P. (2008). Large-scale relocation of two decades of northern California seismicity using cross-correlation and double-difference methods. *Journal of Geophysical Research, 113*, B08311.

Wells, D., & Coppersmith, K. (1994). New empirical relationships among magnitude, rupture length, rupture width, rupture area, and surface displacement. *Bulletin of the Seismological Society of America., 84*, 974–1002.

Wiemer, S., & Katsumata, K. (1999). Spatial variability of seismicity parameters in aftershock zones. *Journal of Geophysical Research, 104*, 13135–13151.

Yagi, Y., & Nishimura, N. (2011). Moment tensor inversion of near-source seismograms. *Bulletin International Institute Seismology Earthquake Engineering, 45*, 133–138.

Yelles-Chaouche, A. K. (2010). *Le Projet SPIRAL: Etude de la structure profonde de la Marge Algérienne: GEOMAG: First congress on the Maghreb Geology, November 10–12.* . Tlemcen.

Yelles-Chaouche, A. K., Abacha, I., Boulahia, O., Aidi, C., Chami, A., Belheouane, A., Rahmani, S. T., & Roubeche, K. (2021). The 13 July 2019 Mw 5.0 Jijel Earthquake, northern Algeria: An indicator of active deformation along the eastern Algerian margin. *Journal of African Earth Sciences*. https://doi.org/10.1016/j.jafrearsci.2021.104149.

Yelles-Chaouche, A. K., Abacha, I, Semmane, F., Beldjoudi, H., & Djellit, H. (2013a). The Beni-Ilmane (North-Central Algeria) earthquake sequence of May 2010. *Pure and Applied Geophysics, 171*, 1283–1298.

Yelles-Chaouche, A. K., Allili, T., Alili, A., Messemen, W., Beldjoudi, H., Semmane, F., Kherroubi, A., Djellit, H., Larbes, Y., Haned, S., Deramchi, A., Amrani, A., Chouiref, A., Chaoui, F., Khellaf, K., & Nait Sidi Said, C. (2013b). The new Algerian Digital Seismic Network (ADSN): towards an earthquake early-warning system. *Advances in Geosciences, 36*, 31–38.

Yelles-Chaouche, A. K., Boudiaf, A., Djellit, H., & Bracene, R. (2006). La tectonique active de la région nord-algérienne. *Comptes Rendus Géosciences, 338*, 1–14.

Yelles-Chaouche, A. K., Djellit, H., Beldjoudi, H., Kherroubi, A., Semmane, F., Haned, A., Allili, T., & Aidi, C. (2009a). Seismicity in northern Algeria: From 419 AD to present. *IASPEI conference, CapeTown (South Africa) January 10–16th, 2009*.

Yelles-Chaouche, A. K., Khelif, M. F., Haned, A., Chami, A., Aidi, C., Beldjoudi, H., Kherroubi, A., & Benaissa, Z. (2018). The Algiers (north-central Algeria) earthquake of August 1st, 2014 Mw 5.5 in the Algiers Bay tectonic context. *Journal of Seismology, 23*, 287–302.

Yelles-Chaouche, A. K., Lammali, K., Mahsas, A., Calais, E., & Briole, P. (2004). Coseismic deformation of the May 21st, 2003, Mw = 6.8 Boumerdes earthquake, Algeria, from GPS measurements. *Geophysical Research Letters, 31*, L13610. https://doi.org/10.1029/2004GL019884.

Yelles-Chaouche, A. K., Roger, J., Deverchere, J., Bracene, R., Domzig, A., Hébert, H., & Kherroubi, A. (2009b). The 1856 Tsunami of Djidjelli (Eastern Algeria): Seismotectonics, Modelling and Hazard Implications for the Algerian Coast. *Pure and Applied Geophysics, 166*, 283–300.

Yelles-Chaouche, A. K., & the Maradja Team. (2006a). A Morphotectonic overview of the deforming seaward boundary of the Africa-Europe convergence zone off Algeria from Oran to Annaba. *EGU Vienna 02–07 April 2006*.

Yelles-Chaouche, A. K., & the Spiral Team. (2010a). From Maradja to Spiral surveys. Recent and active deformation of the Algerian margin and the evidence of contractionnal reactivation. *ESC Montpellier September 2010*.

Ziv, A., & Rubin, A. M. (2000). Static stress transfer and earthquake triggering: No lower threshold insight? *Journal of Geophysical Research, 105*, 13631–13642.